Simulation of Selected Interfacial Dynamic Problems using Cahn-Hilliard Diffuse-Interface Method

by

Hadi Mehrabian

B.Sc., Amirkabir University of Technology, 2003
M.Sc., Sharif University of Technology, 2005

A THESIS SUBMITTED IN PARTIAL FULFILLMENT OF
THE REQUIREMENTS FOR THE DEGREE OF

DOCTOR OF PHILOSOPHY

in

The Faculty of Graduate and Postdoctoral Studies

(Chemical and Biological Engineering)

THE UNIVERSITY OF BRITISH COLUMBIA

(Vancouver)

March 2014

Abstract

Using the Cahn-Hilliard diffuse-interface model, I have studied three interfacial dynamic problems for incompressible immiscible two-phase flows. As the first problem, capillary instability of a liquid torus is computed. The main differences between the torus and a straight thread are the presence of an axial curvature and an external flow field caused by the retraction of the torus. We show that the capillary wave initially grows linearly as on a straight thread. The axial curvature decreases the growth rate of the capillary waves while the external flow enhances it. Breakup depends on the competition of two time scales: one for torus retraction and the other for neck pinch-off. The outcome is determined by the initial amplitude of the disturbance, the thickness of the torus relative to its circumference, and the viscosity ratio.

The second problem concerns interfacial dynamics and three-phase contact line motion of wicking through micropores of two types of geometries: axisymmetric tubes with contractions and expansions of the cross section, and two-dimensional planar channels with a Y-shaped bifurcation. Results show that the liquid meniscus undergoes complex deformation during its passage through contraction and expansion. Pinning of the interface at protruding corners limits the angle of expansion into which wicking is allowed. Capillary competition between branches downstream of a Y-shaped bifurcation may result in arrest of wicking in the wider branch.

As the third problem, auto-ejection of drops from capillary tubes is studied. This study focuses on two related issues: the critical condition for auto-ejection, and the role of geometric parameters in the hydrodynamics. From analyzing the dynamics of the meniscus in the straight tube and the nozzle, we develop a criterion for the onset of auto-ejection based on a Weber number defined at the exit of the nozzle and an effective length that encompasses the geometric features of the tube-nozzle combination. In particular, this criterion shows that ejection is not possible in straight tubes. With steeper contraction in the nozzle, we predict two additional regimes of interfacial rupture: rapid ejection of multiple droplets and air bubble entrapment.

Preface

This PhD thesis entitled ”Simulation of Selected Interfacial Dynamic Problems using the Cahn-Hilliard Diffuse-Interface” presents the main features of the research that I led and carried out during my PhD study under supervision of Professor J. J. Feng. In this preface, the contributions and collaborations to the papers published or submitted for publication from current thesis are briefly explained.

- A version of chapter 3 has been published. H. Mehrabian, and J. J. Feng (2013), Capillary breakup of liquid torus, Journal of Fluid Mechanics 717: 281-292. Under supervision of J. J. Feng, I studied the capillary instability of a liquid torus and drafted the paper. J. J. Feng helped me to prepare the final version of the paper. In addition, I acknowledge discussions with Giovanni Ghigliotti, Ekapop Pairam and Qiming Wang.

- A version of Chapter 4 has been published. H. Mehrabian, P. Gao, and J. J. Feng (2011), Wicking flow through microchannels. Phys. of Fluids 23: 122108. Under supervision of J. J. Feng, I studied wicking flow inside two type of geometries: axisymmetric area change and Y-shape 2D branching and drafted the paper. J. J. Feng helped me to prepare the final version of the paper.

- A version of Chapter 5 has been prepared for submission. I conducted this study under supervision of J.J. Feng. The final version of the manuscript was prepared with help of J. J. Feng. I would thank Andrew Wollman for generously providing data and video of his experiments to me.

Table of Contents

List of Figures

Nomenclature

Symbol	Units (SI)	Description
A	m^2	Solid surface
a_n	$--$	Radius of thickest part of the torus cross section
a_t	$--$	Radius of thinnest part of the torus cross section
a_0	m	Initial radius of torus cross section
a_0^{-1}	m^{-1}	Azimuthal curvature of the torus
$a(t)$	m	Instantaneous radius of torus cross section
Bo	$--$	Bond number
C	$--$	Contraction ratio of the nozzle
Ca	$--$	Capillary number
Cn	$--$	Cahn number
d	m	distance between the droplet and the meniscus
D_e	m	Effective width
D_1	m	Diameter of wide branch
D_2	m	Diameter of narrow branch
D_0	m	Diameter of root tube
E	$N.m$	Energy inside the tube-nozzle-reservoir combination
$\mathcal{F}$	$N.m$	Total free energy
f_{mix}	N/m^2	Mixing energy of fluid-fluid system
f_w	N/m	Wall energy
G	N/m^2	Chemical potential
G_p	$--$	Grading parameter
H_b	m	Position of the center of the meniscus
H_c	m	Position of the center of the meniscus
H_t	m	Total length
H_u	m	Length of upstream section
$H(t)$	m	Instantaneous height of the liquid column
H_w	m	Position of the meniscus wall point
H_0	m	Initial position of the meniscus
h_1	$--$	Mesh size at the interface
h_2, h_3	$--$	Mesh sizes in two bulks
k	$--$	Wavenumber of the disturbance

$\bar{l}(t)$	m	Instantaneous wavelength of the disturbance
$\bar{l}_0$	m	Initial wavelength of the disturbance
l_0	$--$	Dimensionless initial wavelength of the disturbance
l	$--$	Dimensionless wavelength of the disturbance
l_c	m	Characteristic length scale
l_d	m	Diffusion length scale
L_e	$--$	Effective length
L_j	$--$	Length of the jet
L_n^c	$--$	Critical length in narrow branch
L_n	$--$	Length of liquid column in narrow branch
L_w	$--$	Position of the contact line (Chapter 5)
L_w	$--$	Length of liquid column in wide branch (Chapter 4)
L_0	m	Initial position of the interface
m	$--$	Viscosity ratio
$\mathbf{n}$	$--$	Unit normal vector
N	$--$	Number of produced droplets (Chapter 3)
N	$--$	Number of contraction-expansion cycles (Chapter 4)
Oh	$--$	Ohnesorge number
p	N/m^2	Pressure
p_a	N/m^2	Ambient pressure
p_j	N/m^2	Pressure at junction
p_n	N/m^2	Pressure at the narrower branch in Chapter 4
p_n	N/m^2	Pressure at the nozzle exit in Chapter 5
p_w	N/m^2	Pressure at the wider branch
R	m	Equivalent drop radius (Chapter 2)
R_b	m	Radius of entrapped bubble
R	m	Radius of the tube
R_n	m	Radius of the nozzle
$R(t)$	m	Instantaneous axial radius of the torus
R_0	m	Initial axial radius of the torus
R_0^{-1}	m^{-1}	Initial axial curvature of the torus
R_1	m	Radius of narrower section
R_2	m	Radius of the wider section
r, z, ω		Cylindrical coordinates
S	$--$	Dimensionless diffusion length
t	$--$	time
t^c	$--$	Critical time for flow in wide branch
t_c	sec	Capillary time scale
t_{ci}	sec	Capillary-inertial time

t_p	sec	Pinch-off time of the torus (Chapter 3)
t_p	$--$	Passage time (Chapter 4)
t_s	sec	Shrinkage time of the torus
t^*	$--$	Time with respect to contact line pinning moment
U	m/sec	Impact velocity
$\mathbf{v}$	m/sec	Velocity vector
v_{ci}	m/sec	Capillary-inertial velocity
V_c	$--$	Velocity of the center of the meniscus
V_n	$--$	Average velocity at the nozzle exit
V_w	$--$	Velocity of the contact line
v_{WL}	m/sec	Lucas-Washburn velocity
V_0	m/sec	Average velocity in root tube
V_1	m/sec	Average velocity in wider branch
V_2	m/sec	Average velocity in narrower branch
We	$--$	Weber number
W_l	m	Width of the lip

Greek symbols

Symbol	**Units (SI)**	**Description**
β	$--$	Torus aspect ratio (Chapter 1 and 3)
β	$--$	Expansion angle of the Y-branching (Chapter 4)
μ	$Pa.sec$	Viscosity
μ_a	$Pa.sec$	Viscosity of the air
μ_m	$Pa.sec$	Viscosity of the surrounding medium
μ_t	$Pa.sec$	Viscosity of the torus
ρ	$kg.m^{-3}$	Density of the fluid
ρ_a	$kg.m^{-3}$	Density of the air
ρ_s	m	Radius of spherical surface
σ	N/m	Interfacial tension
σ_{w1}, σ_{w2}	N/m	Solid-liquid Interfacial tensions
Ω	m^3	fluid domain
α	$--$	Growth rate of the disturbance (Chapter 3)
α	$--$	Contraction or expansion angle (Chapters 4 and 5)
α_m	sec^{-1}	Growth rate of fastest growing wavelength
α_M	$--$	Ratio of growth rate terms in Eq. 49 of Ref. [53]
α_r	$--$	Ratio between growth rate on a torus and straight filament
δ	$--$	Instantaneous amplitude of the disturbance
δ_c	$--$	Critical amplitude of the disturbance

δ_m	m	Height of the meniscus
δ_0	$--$	Initial amplitude of the disturbance
κ	$1/m$	Effective curvature
ϕ	$--$	Phase field parameter
λ	N	Mixing energy density
θ	$--$	Static contact angle
θ_b	$--$	Breakthrough angle
θ_d	$--$	Dynamic contact angle
θ_l	$--$	Static contact angle on the lip
θ_m	$--$	Maximum angle that interface can reach in the corner
ϵ	m	Interfacial thickness
Π	$--$	Wall relaxation
γ	$m^4/N.sec$	Mobility parameter
Γ	$m/N.sec$	Rate of wall relaxation

List of Abbreviations

GRUMMP	Generation and Refinement of Unstructured Mixed-Element Meshes in Parallel
AMPHI	Adaptive Meshing using a Phase Field (ϕ)
GDM	Gas Diffusion Medium

Acknowledgements

I would like to express my special appreciation and thanks to my advisor professor James J. Feng, who has been a tremendous mentor for me. His expertise, devotion to research, sense of responsibility and kindness helped me to grow as a research scientist.

A special thanks to my family. Words cannot express how grateful I am to my mother and father for all of the sacrifices that they have made on my behalf and for all the prayers that sustained me through my life; and to my mother-in law and father-in-law, whose support and encouragement was a big asset for me during these years. At the end, I would like express my sincerest appreciation to my beloved wife and best friend Faezeh whose love and patience enabled me to finish this thesis.

Chapter 1

Introduction

1.1 Motivation

The category of problems in which the interaction between forces created by the surface and bulk flow is important is called interfacial hydrodynamics. Beside being scientifically interesting, in recent years due to increasing interest in small scale applications (like micro-engineering), interfacial flow has assumed greater significance. Using the Cahn-Hilliard diffuse interface method, we are going to numerically study the following problems:

- Capillary breakup of a liquid torus
- Wicking flow through microchannels
- Auto-ejection of liquid drops from capillary tubes

These problems have been selected based on several considerations. First, in the framework of immiscible mixtures of incompressible Newtonian fluids, we are interested in fundamental scientific questions about the dynamics of the interface. Second, these questions, while scientifically significant, must be computationally amenable to our numerical algorithms and codes. Typically, the thickness of the interface in diffuse-interface method should be two orders of magnitude smaller than the bulk to produce physically meaningful results. This gives rise to high computational cost and limits the amount of inetrfacial area/length of the problem especially for three dimensional configurations. Third, for the problems with moving contact lines, there should be an experimental or a theoretical datum to calibrate the parameters of the numerical model (see section §2.2 for more details).

Here, a brief introduction for each problem and numerical method is presented. More detailed description of the studied problems and method is presented in the corresponding sections.

As the first problem, we will study the capillary instability of a Newtonian liquid torus suspended in a surrounding Newtonian liquid. This study is motivated by the recent experiment of Pairam and Fernandez-Nieves [57]

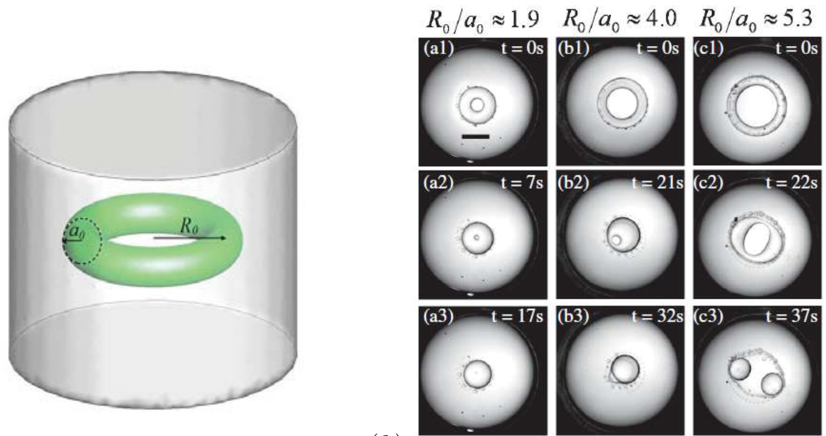

(a) (b)

Figure 1.1: (a) Schematic of a liquid torus suspended in a bath of surrounding liquid (b) Experimental results of [57] on the breakup of silicone-oil tori suspended in glycerine. The thin torus breaks down into multiple droplets while the fat torus shrinks into one droplet.

on the breakup of silicone-oil tori suspended in glycerine. As shown in Fig.1.1(b), they observed that a torus can either shrink to a single droplet or break down into multiple droplets depending on the ratio of its axial radius R_0 to the radius of its cross section a_0 (Fig.1.1(a)). There is a clear connection to the classical problem of Rayleigh-Tomokita instability [65, 81] of a straight, infinitely long filament for which the growth rate depends on the wavenumber, defined relative to the radius of the filament and also its viscosity ratio. With the torus, several complications arise. First, due to periodicity of the torus geometry only a few discrete wavelengths are possible on a torus of given aspect ratio $\beta = R_0/a_0$. Second, the torus has an axial curvature which may affect the growth of the capillary wave. In addition, axial curvature produces shrinkage which induces flow in the surrounding fluid which may modify the capillary instability as well [52, 81]. Finally the presence of the shrinkage puts a limitation on the available time for the disturbance growth. Here we are going to explore the effect of these differences on the initial growth of small disturbances as well as final breakup and number of produced droplets.

The second problem concerns wicking flow through microchannels. Wicking is the suction of a liquid by the negative capillary pressure due to the meniscus curvature. It is a key mechanism for flow in porous media [21] like water transport in the gas diffusion medium of proton-exchange-membrane fuel cells [54], and in microfluidics for chemical analysis and biological assay [10, 17]. Porous media and microfluidics devices can have a complex microchannel structure through which flow happens in a range of different geometrical configurations where the interfacial morphology and motion determine to a large degree the efficacy and efficiency of the devices [10, 17]. Two types of common geometrical features of microchannels are contraction or expansion in the tube area and interconnectivity of the channels. The focus of this study is to investigate the interfacial dynamics in a simplified form of these two geometries.

Effect of area change on the meniscus dynamics has been studied before [47, 60, 66, 68, 73]. These studies are generalizations of the Lucas-Washburn solution to tubes and channels of gradually varying cross sections. However, a common feature of all these studies is that they ignore dynamics at the meniscus. The capillary pressure is quasi-statically equilibrated along the meniscus, thus giving it a spherical shape whose curvature is used to compute the capillary pressure via the Young-Laplace equation. Such assumption is not valid in relatively sharp area changes and the transient dynamics of the meniscus needs to be considered. As is shown in Fig.1.2, here we will consider an axisymmetric contraction, expansion and combination of them and study the dynamics of an interface through these geometries. Competition among interconnected pores is considered the key mechanism in developing a tree-like morphology of water transport in the gas diffusion medium (GDM) of fuel cells [54, 59]. To the best of our knowledge such dynamics has not been studied for wicking flow. Therefore we are going to consider a two-dimensional Y-shaped branching configuration and study the interfacial dynamics on and after the junction.

As the third problem, we have studied the *auto-ejection* of drops from capillary tubes. The term auto-ejection is used by Wollman and coworkers for a new mode of drop formation that relies on wicking in a capillary tube [86, 87, 88]. As shown in Fig. 1.3, a glass tube with a tapered end is put into contact with a reservoir of silicone oil, which wets the glass perfectly. The liquid meniscus rises with sufficient momentum such that a jet is ejected from the nozzle, and later disintegrates into droplets. The sequence of photos shown here were captured under microgravity in a drop tower [88]. Similar experiments have been done in the International Space Station and under normal gravity on earth [86, 87]. The process is interesting in that it involves no external forces or flux, and is entirely autonomous.

The critical condition for ejection is the most important question about the auto-ejection process. Wollman et al. [88] have suggested an instan-

Figure 1.2: Schematic of an axisymmetric contraction and expansion in tube area.

taneous Weber number at the end of the nozzle as the parameter which controls the ejection. Experimental data of Wollman and Weislogel [88] shows that such Weber number is not sufficient to quantify the number of ejected droplets. There is a large scatter of data in terms of the instantaneous Weber number.

Another important question is to elucidate the role of the geometric parameters on the auto-ejection. Dynamics of auto-ejection happens through two main stages. The first stage is meniscus rise inside the tube and nozzle. It is governed by interplay between contact line dynamics, inertia and viscous forces which are themselves a function of the geometric parameters and liquid-solid properties. The second stage of liquid ejection from the tube is governed by the interplay between incoming inertia and capillary forces. Unlike pulsed ejection in which there is an imposed source of force or velocity, in capillary ejection velocity decreases as liquid moves out of the tube. Variation of velocity as well as its profile at the nozzle exit depends on the geometric parameters and fluid-solid properties. The aim of this study is to develop a criterion for auto-ejection and to study the role of geometric parameters as typically used in experiments.

There are theoretical and numerical difficulties in computing interfacial dynamics. These include the lack of a good model for the moving contact line, the need to capture dynamically a moving and deforming interface, morphological singularities in coalescence and rupture of interfaces, and the complex flow geometries in practically interesting problems like flow

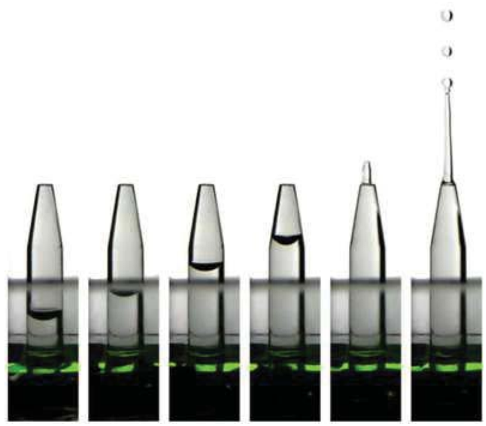

Figure 1.3: A sequence of snapshots showing spontaneous capillary rise and auto-ejection of droplets in the experiment of [88] under microgravity. The inner diameter of the glass tube is 9.2 mm in the straight section, and the liquid is PDMS of viscosity 0.65 cs. The drop volume is roughly 20 μl. Ohnesorge number $Oh = 0.0015$, static contact angle $\theta = 0^o$, contraction angle of nozzle $\alpha = 17^o$, contraction ratio of nozzle $C = 0.42$, tube length $L = 8.0$ (see § 5.2 for detailed definition of the terms α, C, Oh, and L). The photos are taken 0.1 s apart. Adapted from [88] with permission, ©Springer.

in porous medium. The Cahn-Hilliard diffuse-interface method is a powerful method in treating such difficulties. As real interfaces are actually thin mixing layers, in this method an interface has a finite thickness and stores a mixing energy. The two phases are distinguished by a phase field parameter that varies smoothly through the interface. When the interface thickness goes to zero the model approaches a sharp-interface level set formulation.

An advantage of using the diffuse-interface method is that it regularizes the singular events on the interfaces like breakup, coalescence and moving contact lines. Thus, this formulation allows us to capture the moving interface and its morphological changes accurately and naturally, including pinning at sharp corners and otherwise singular interfacial breakup at bifurcations without manual interventions. In the aforementioned problems, the physical origin of the method can also shed additional light on the underlying physics.

1.2 Thesis outline

In Chapter 2, the Cahn-Hilliard diffuse-interface method is introduced and the way that the moving contact line is captured in this model is explained. The key features of the finite element solver are explained and finally, two common difficulties in using the Cahn-Hilliard diffuse-interface method are explained in the context of an example problem. Chapters 3 to 5, deal with the three interfacial dynamics problems to be studied. In Chapter 3, we report simulation results for the dynamics of a Newtonian torus suspended in a surrounding Newtonian liquid in three dimensions (3D). This study has three man parts. First we will study the linear growth of a sinusoidal disturbance on the torus and investigate the effect of the retraction and the axial curvature on the growth rate. Then we will examine the nonlinear instability and the final breakup into droplets in terms of competition between retraction and pinch-off mechanism. Finally the numerical results will be compared with the experiment.

In Chapter 4, we report numerical simulations of wicking through micropores of two types of geometries, axisymmetric tubes with contractions and expansions of the cross section, and two-dimensional planar channels with a Y-shaped bifurcation. At a contraction and an expansion, the dynamics of the meniscus at concave and convex corners is illustrated and its effect on passage time is discussed. For branching geometries, dependence of the flow trajectory on geometrical and wetting properties of conduits is explained.

In Chapter 5, the auto-ejection of drops and jets from capillary tubes is investigated. A criterion for ejection is developed in terms of the instantaneous Weber number at the nozzle exit and the effective tube length. Effects of a large contraction angle on the meniscus dynamics inside the nozzle and on the auto-ejection are studied. Finally, the effect of the thickness of the tube wall on ejection is explained.

Finally, Chapter 6 summarizes the thesis, outlines the significance and limitations of the current work, and makes recommendations for future work.

Chapter 2

Methodology of Research

2.1 Governing equations

The problems that we have chosen to study all fall in the category of immiscible two-phase flows with both fluids being Newtonian. The flow hydrodynamics is governed by the continuity equation (2.1) and momentum equation (2.2) for incompressible flows:

$$\nabla \cdot \boldsymbol{v} = 0, \tag{2.1}$$

$$\rho \frac{D\boldsymbol{v}}{Dt} = -\nabla p + \nabla \cdot (\mu \nabla \boldsymbol{v}) + G \nabla \phi, \tag{2.2}$$

where $\boldsymbol{v}$ is the velocity, p is the pressure, ρ is the density, and μ is viscosity. The term $G\nabla\phi$ in equation (2.2) represents the role of interfacial tension in the momentum equation [39, 97] and is obtained by means of variational calculus. This is the way that a diffuse-interface model handles the interface, as will be explained below. For the first two problems the Bond number is very small and the third problem, on auto-ejection from a capillary tube, concerns mostly microgravity experiments. Thus, gravity is ignored in most of the simulations to be presented. In the first two problems considered here the resulting Reynolds number is typically much below unity and the flow dynamics is governed by capillary and viscous forces. Therefore, we will neglect the inertia term (left hand side of equation 2.2) for the first two problems and solve the modified form of the Stokes equation. For the third problem, viscous forces are negligible and the flow dynamics is determined by the balance between capillary and inertial forces.

To capture the interface, the Cahn-Hilliard diffuse-interface method is used. In the diffuse-interface model the two fluid components are viewed as mixing to a limited extent in a narrow interfacial layer. A scalar *phase field* ϕ is introduced to distinguish the components such that $\phi = 1$ in one liquid, $\phi = -1$ in the other liquid or gas, and $\phi = 0$ gives the position of the interface. In this framework all flow parameters are continuous through the interface and instead of solving equations for two parts of the domain separated by the interface, the same equations are solved for the whole domain including the interface itself. In the interfacial region, $\boldsymbol{v}$ may be viewed as a volume-averaged velocity and μ as an average viscosity between those of the two components:

$$\mu = \frac{1+\phi}{2}\mu_1 + \frac{1-\phi}{2}\mu_2. \tag{2.3}$$

The Cahn-Hilliard model is an energy-based approach to the diffuse-interface method. The total free energy of the system can be written in the following form

$$\mathcal{F} = \int_\Omega f_{mix}(\phi, \nabla\phi) d\Omega + \int_A f_w(\phi) dA, \tag{2.4}$$

where Ω is the fluid domain and A is the solid surface, and f_{mix} is the mixing energy of the fluid-fluid system

$$f_{mix}(\phi, \nabla\phi) = \frac{\lambda\,|\nabla\phi|^2}{2} + \frac{\lambda}{4\epsilon^2}(\phi^2-1)^2, \tag{2.5}$$

where ϵ is the interfacial thickness and λ is the mixing energy density. In the limit of thin interfaces, the classical concept of interfacial tension σ can be recovered from the mixing energy:

$$\sigma = \frac{2\sqrt{2}}{3}\frac{\lambda}{\epsilon}. \tag{2.6}$$

f_w in 2.4 is the wall energy [40]:

$$f_w(\phi) = -\sigma\cos\theta\frac{\phi(3-\phi^2)}{4} + \frac{\sigma_{w1}+\sigma_{w2}}{2}, \tag{2.7}$$

At $\phi = \pm 1$, i.e. away from the contact line, f_w should give the fluid-wall interfacial tension for the two fluids, σ_{w1} and σ_{w2}. This requirement leads to Young's equation that prescribes the static contact angle θ:

$$\cos\theta = \frac{\sigma_{w2}-\sigma_{w1}}{\sigma}. \tag{2.8}$$

Using variational calculus, we can calculate the chemical potential as the variation of the mixing energy with respect to ϕ:

$$G = -\lambda\nabla^2\phi + \frac{\lambda}{\epsilon^2}\phi(\phi^2-1). \tag{2.9}$$

Using the gradient of the chemical potential to drive the diffusive fluxes across the interface, the Cahn-Hilliard equation for the evolution of ϕ is derived [13]:

$$\frac{\partial \phi}{\partial t} + \boldsymbol{v} \cdot \nabla \phi = \nabla \cdot (\gamma \nabla G), \tag{2.10}$$

where γ is the mobility parameter and assumed to be constant. Flow hydrodynamics and interface dynamics is obtained by solving equation (2.10) along with equation (2.1) and (2.2) as a boundary value problem, with boundary conditions specified below.

2.1.1 Simulation of moving contact lines

Problems studied in Chapter 4 and Chapter 5 involve contact line dynamics. Interaction of molecular and large scale dynamics at the three phase contact line makes it a stress singularity point for Navier-Stokes formulation. Different methods use different approaches to handle it. Traditional sharp-interface models typically impose a slip velocity on the wall [102]. Therefore, it is important to explain how the contact line dynamics is captured in the Cahn-Hilliard diffuse-interface method.

In the diffuse-interface method diffusion across the interface driven by the gradient of chemical potential (G) allows the contact line movement without imposing a slip velocity on the wall. This has two implications, first it is possible to use no-slip boundary condition on the wall (equation 2.13). Second, the mobility parameter in equation (2.10) has an important role in contact line movement which will be discussed in the next section.

Physically it is known that the interface at the wall is almost at equilibrium. In the Cahn-Hilliard model, fluid-fluid and solid-fluid intermolecular forces are reflected in mixing energy and wall energy respectively. In most situations, the fluid layer next to the wall is assumed to be always in equilibrium with the wall. Mathematically this is reflected by a natural boundary condition [40, 96]

$$\boldsymbol{n} \cdot \nabla \phi = -\frac{f_w'(\phi)}{\lambda}, \tag{2.11}$$

where the normal vector $\boldsymbol{n}$ points into the solid wall. It is also possible to allow the wall energy to relax at a finite rate. This leads to another boundary condition (equation 2.12) in which Γ is the rate constant of wall relaxation

$$\boldsymbol{n} \cdot \nabla \phi = -\frac{f_w'(\phi)}{\lambda} - \frac{1}{\Gamma \lambda}\left(\frac{\partial \phi}{\partial t} + \boldsymbol{v} \cdot \nabla \phi\right). \tag{2.12}$$

For $\Gamma \to \infty$, it can be shown that to the leading order, equation (2.12) constrains the dynamic contact angle to be equal to the static one [40, 93]. Either of the two equations above, along with the no-slip condition and zero mass flux into the wall,

$$\boldsymbol{v} = 0, \tag{2.13}$$
$$\boldsymbol{n} \cdot \nabla G = 0, \tag{2.14}$$

gives the complete set of boundary conditions for the flow problem.

2.2 Parameters of the Cahn-Hilliard model

The Cahn-Hilliard model formulated above has three parameters that have no counterparts in conventional Navier-Stokes problems. The interfacial thickness ϵ, mobility parameter γ, and rate of wall relaxation Γ. They give rise to three additional dimensionless parameters: the Cahn number $Cn = \epsilon/l_c$, diffusion length scale $S = l_d/l_c$, and wall relaxation $\Pi = 1/\Gamma\mu l_c$. Cn is the ratio between the interfacial thickness and the macroscopic length scale (l_c), S is the ratio of the *diffusion length* $l_d = \gamma^{1/2}(\mu_1\mu_2)^{1/4}$ to the macroscopic length [96], and Π shows how fast flow close to the wall equilibrates with the wall. The choice of these three parameters (Cn, S, and Π) is informed by their physical meanings and the requirement of achieving the sharp-interface limit. Real interfaces, a few nanometers in thickness, are typically not resolvable in macroscopic flow simulation. Thus the diffuse-interface method uses an artificial ϵ that may be much larger than the real value. This is allowable if the sharp-interface limit is achieved: when ϵ and Cn are sufficiently small such that the results are not affected by the unrealistic thickness of the interface [12, 96]. For interfacial flows without contact lines such as the capillary instability of a suspended torus, the sharp-interface limit is typically approached at $Cn \sim 0.01$ [97]. In such flows the Cahn-Hilliard diffusion across the interface, represented by l_d or S, is immaterial as long as the sharp-interface limit is achieved.

With moving contact lines, Yue *et al.* [96] have shown that the achievement of sharp-interface limit is also dependent on the diffusion length. For Couette and Poiseuille flows with a transverse interface, they found that the shape of the meniscus converges to a unique solution after Cn falls below a threshold $Cn \approx 4S$ and suggested this as the criterion for achieving the sharp-interface limit. On the other hand, the motion of the contact lines is affected by interfacial diffusion and wall relaxation. Thus, S and Π must be chosen judiciously, e.g., to coincide with an experimental measurement

[96]. We use the following procedure proposed by Yue and Feng [93] to set values of S and Π. Choose as small an Cn value as computationally affordable, and then pick a value for S to ensure the sharp-interface limit is achieved. Finally, determine the wall relaxation parameter Π by fitting an experimental datum. For studying the wicking flow, contact line movement happens very slowly and meniscus keeps its equilibrium shape. Therefore we have set Π equal to zero for the problem studied in Chapter 4. For the auto-ejection problem, due to fast movement of the meniscus, there is a considerable deviation from the static shape and Π should have a non-zero value.

2.3 Discretization of governing equations and computational domain

The governing equations are solved using a finite-element package called AMPHI in planar 2D, axisymmetric and 3D geometries. [97] and [100] have described the numerical algorithm in detail, presented numerical experiments on grid and time-step refinements and validated the methodology against numerical benchmarks. The numerical package has been applied to a number of interfacial-dynamics simulations [1, 27, 28, 96, 101]. Here, we will only mention a few important features.

The discretization of the governing equations follows Galerkin formalism. The fourth-order Cahn-Hilliard equation is decomposed into two second-order equations:

$$\frac{\partial \phi}{\partial t} + \boldsymbol{v} \cdot \nabla \phi = \frac{\gamma \lambda}{\epsilon^2} \nabla^2 (\psi + s\phi), \quad \psi = -\epsilon^2 \nabla^2 \phi + (\phi^2 - 1 - s)\phi, \tag{2.15}$$

where s is a positive number to enhance the stability of the numerical method and set to 0.5 [69]. Piecewise quadratic (P2) elements are used for velocity, ϕ and ψ and piecewise linear (P1) elements are used for pressure. Time-stepping is done in a second-order implicit scheme. The nonlinear algebraic system generated from the weak form of the equations is solved using Newton's method. The equations are discretized on an unstructured grid and the finite thickness of the interface is resolved using adaptive meshing, with the grid being dynamically refined and coarsened, respectively, upstream and downstream of the moving interface. This is done by a general-purpose mesh generator called GRUMMP that produces a triangular mesh in 2D and a tetrahedral mesh in 3D [26] by Delaunay triangulation. It controls the grid size by using a scalar field, which can easily be computed from the $\nabla\phi$ field of the diffuse-interface method.

Four parameters are used to specify the domain discretization: mesh size at the interface (h_1), mesh sizes at the two bulks (h_2 and h_3), and a grading parameter (G_p) which controls the transition between the bulk and interface mesh size. For all of the results to be presented, we have used sufficiently refined spatial and temporal discretization to ensure numerical convergence. This is confirmed by grid and time-step refinements to verify that the results change little with further refinement. A few typical spatial and time steps are indicated below as examples. For capillary breakup of liquid torus (Chapter 3), mesh sizes inside the torus, at the interface, and in the surrounding liquid are chosen to be equal to 1/5 of the torus thickness, interfacial thickness (ϵ), and 1/2 of torus thickness, respectively. Grading parameter G_p is chosen to be 3. For wicking flow in microchannel (Chapter 4) and auto-ejection of drops from capillary tubes (Chapter 5), the bulk mesh sizes inside the tube and nozzle are chosen to be 1/8 of the tube and nozzle exit radii, respectively. Mesh size at the interface is chosen to be $\epsilon/2$ and grading parameter for these problems is equal to 5. The typical time-step of the simulations for problems in Chapters 3, Chapter 4, and Chapter 5 is 10^{-2}, 5×10^{-3}, and 5×10^{-4}, respectively.

2.4 Limitations on resolving small lenght scales

In this section two types of difficulties in using the Cahn-Hilliard diffuse-interface model will be discussed. These difficulties happen due to limitations on resolving the small length scales which are not specific to the Cahn-Hilliard model. The real diffusion length of the contact line is around six orders of magnitude smaller than the bulk length scale which is not computationally resolvable. Therefore, there are two parameters in the model γ, Γ whose values are not known and they are important to the contact line dynamics. To capture the interfacial dynamics using a large diffusion length, it is required to calibrate the diffuse-interface parameters using an experimental or a theoretical data point. Such data points are not available for all physical problems.

The second difficulty, is the high computational cost of the diffuse-interface method. Numerically capturing an interfacial region which is around six orders of magnitude smaller than bulk region is almost impossible with current computational resources. Therefore, the sharp-interface concept is used to show that with much thicker interfaces, it is possible to get physically meaningful and numerically converged results. Despite being a remedy for many interfacial problems, such an approach fails when there are disparate length scales in the problem which are important to the final output of the simulation. An example is to capture the physical quantities which are very sensitive to coalescence/pinch-off phenomenon. Physically such a process depends on the intermolecular forces. Sharp-interface methods face a singularity in dealing with coalescence/pinch-off which is usually handled by imposing a cut-off length. In the diffuse-interface method, there is no need to impose an extra cut-off condition and such length is determined by the diffusive nature of the method and finite thickness of the interface. For some problems such natural treatment of the coalescence/pinch-off is desirable like the filament breakup for capillary instability of a torus (Chapter 3), and droplet pinch-off for the auto-ejection (Chapter 5). But sometimes the desired physical quantity is strongly dependent on the inherent cut-off length of the diffuse-interface method. One such quantity may be, for example, the duration of a drop pinch-off process. As the characteristic length scale eventually goes to zero, no numerical scheme can follow the process "exactly" till the end. In reality, short-range molecular effects come in at some point to dominate the rest of the process. Then it is a subtle point as to how a diffuse-interface model might represent such a process. In the following, we illustrate both difficulties by a concrete example.

2.4.1 Bubble production in meniscus sessile droplet collision

Let's apply the Cahn-Hilliard diffuse-interface method to study air-entrapment when a nearly flat liquid meniscus impacts a sessile droplet. Such an impact may happen in dip-coating [6, 19], immersion lithography [75] and results in a production of small air bubbles which are not desirable. Keij et al. [43] have studied this problem experimentally and showed that when an interface impacts a sessile droplet, there are two possible scenarios: coalescence of the droplet and meniscus on or close to the contact line and coalescence farther above the substrate. The first case will result in either no air bubble formation or appearance of a floating air bubble. The second case produces a bubble that sticks to the substrate. It is shown that the size of the floating bubble increases with increasing the capillary number and the size of sticking bubbles is independent from the impact velocity and is about an order of magnitude smaller than the first.

We aimed to carry out numerical simulations in both two (Fig. 2.1(a)) and three dimensional setup (Fig. 2.1(b)) in which a meniscus with a velocity U and contact angle of θ will impact a sessile droplet with equivalent radius R. As is shown in Fig. 2.1(a) a simple shear flow is imposed at the inlet

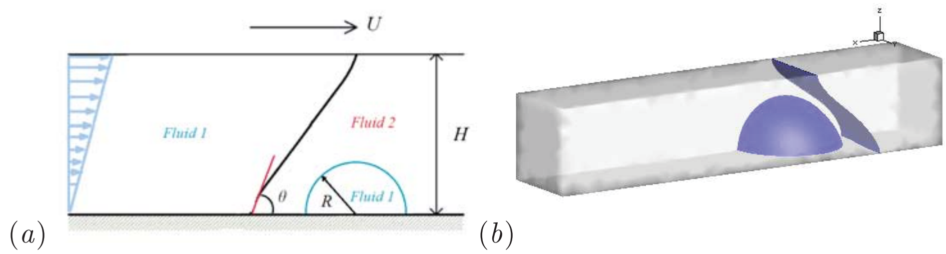

Figure 2.1: (a) A meniscus with a velocity U and contact angle of θ will impact a sessile droplet with a equivalent radius R (b) Three dimensional schematic of the problem setup.

and it is assumed that the meniscus has reached its steady shape before the impact. The nondimensioanl parameters of the problem are capillary number, viscosity ratio, contact angle, and gap size. The main desired output is how the coalescence, bubble shape and its volume vary with the governing parameters. We also assume rapid relaxation of the wall energy so Π is equal to zero. We were unsuccessful in simulating both floating and sticking bubbles, reasons for which are explained in the following sections.

2.4.2 Dependence of bubble dynamics on meniscus shape

The main result that we want to capture in this study is the bubble size and its position, which depend on whether the coalescence between the meniscus and the drop happens on the wall or at some point above the wall [43]. Position of the coalescence is dependent on the shape of the meniscus which itself is dependent on the value of the diffusion length scale. It is shown by Yue *et al.* [96] that in shear flows the meniscus shape or interface inclination is highly sensitive to S. In Fig. 2.2, meniscus shapes for two different values of the diffusion length scale are shown. It can be easily seen that at S=0.0025, collision on the substrate never happens while for S=0.04, drop and meniscus will collide on some point above the meniscus. In addition, the amount of the air trapped in the bubble depends on the shape of the meniscus. This means that a slight change in the value of the diffusion length can change the shape of the meniscus and hence the type of the coalescence and the size of the bubble considerably. Therefore in order to get physically meaningful results, it is very important to have a good estimate for the value of S based on an experimental datum. The experimental data point is available for a case in which the bubble size is at

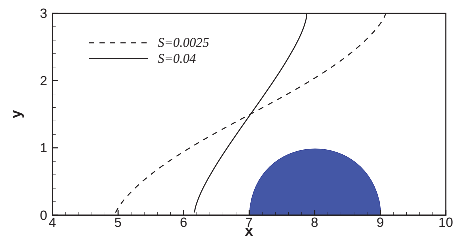

Figure 2.2: Effect of diffusion length scale on the coalescence type.

least ten times smaller than the drop radius. This brings us to the second difficulty which is discussed in the next section.

2.4.3 Dependence of bubble volume on cut-off length

As mentioned before, the important quantity that we want to capture is the volume for the bubble, which equals the amount of air entrapped between the meniscus and the droplet. Therefore, the distance between droplet and meniscus (d) at the moment of pinch-off determines the volume of the bubble. If we assume that air entrapped between the droplet and interface is an air sheet with the thickness d and area equal to the front face of the droplet, then the radius of the bubble can be roughly related to the distance between the meniscus and droplet as

$$\frac{R_b}{R} \approx \left(\frac{d}{R}\right)^{\frac{1}{3}} \tag{2.16}$$

where R_b is the radius of the bubble. The largest reported bubble size in the experiment is around one tenth of the droplet size. Therefore, to capture such bubble size d/R ratio should be at least 1×10^{-3}. According to numerical results, two interfaces start affecting each other when they are approximately 5ϵ apart (ϵ is the interface thickness) for $S = 0.01$. This means that the Cn number should be around 2×10^{-4}. The smallest possible Cn achievable in 3D simulation is 0.015. Therefore, capturing such small bubble size is impossible with current computational resources.

Problems to be studied in Chapter 3 to Chapter 5, are not subjected to the mentioned difficulties where obtained results are not sensitive to the pinch-off/coalescence time/length scale. Problems in Chapters 4 and 5 involve contact line movement for which there are theoretical and experimental data points respectively.

Chapter 3

Capillary Breakup of a Liquid Torus

3.1 Introduction

As discussed in Chapter 1, we want to study the capillary breakup of a liquid ring suspended in a surrounding liquid which has a main additional geometric characteristic compared to a straight filament: the presence of axial curvature around the center of the torus. The axial curvature modifies the curvature driven capillary instability and produces shrinkage which imposes an external flow around the torus, changes the instantaneous geometry of torus and puts a time limitation on disturbance growth.

The initial growth rate of the disturbances can be related to linear growth rate of the liquid filament which is a classical problem in fluid mechanics [24, 71]. A long cylindrical liquid thread becomes linearly unstable to disturbances with a wavelength longer than the circumference of the thread $2\pi a$, a being the radius of the filament. The most unstable wavelength is $9.02a$ for an inviscid filament [65], and longer and dependent on the viscosity ratio for a viscous thread in a viscous surrounding fluid [80]. The capillary waves grow into the nonlinear regime and ultimately lead to breakup, and satellite drops may appear depending on the viscosity ratio [79]. Thus, capillary breakup of long straight filaments is well understood.

In comparison, we have a rather limited knowledge of the stability of curved filaments. Experimentally, Pairam and Fernandez-Nieves [57] studied the retraction and breakup of Newtonian tori in a Newtonian surrounding liquid. McGraw et al. [50] and Wu et al. [89] further considered the breakup of nano-scale polymer and liquid metal rings on solid substrates. Several theoretical and numerical studies have appeared in the literature, and most of these have dealt with the more complicated situation of a liquid ring or torus in contact with solid substrates. For instance, Wu [90] computed the Rayleigh modes on a liquid ring spreading on a solid after impingement. Bostwick and Steen [9] considered the static stability of the

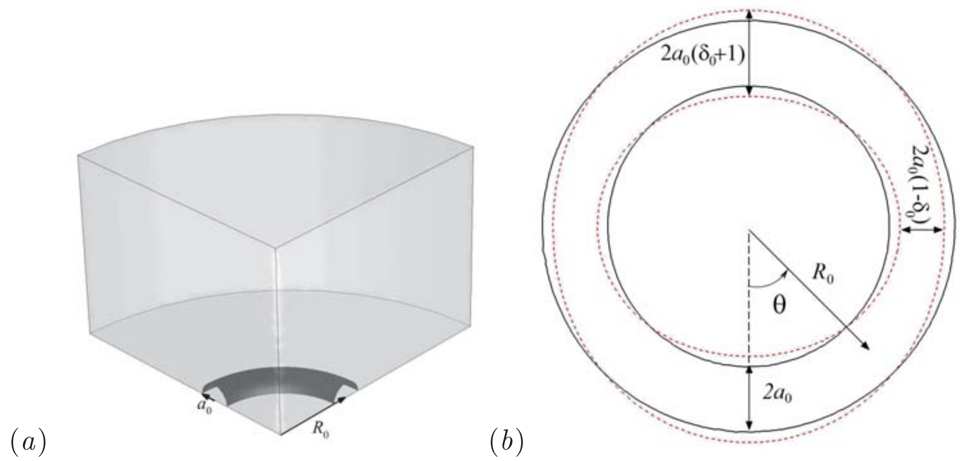

Figure 3.1: (*a*) A quarter of the top half of a liquid torus for simulating the capillary growth of an even mode, i.e. with an even number of wavelengths around the torus. For odd modes, a half of the top half must be included. (*b*) The interface on the symmetric mid-plane with and without a sinusoidal disturbance.

so-called torus lift, a liquid ring constrained by a solid ribbon in contact with part of the liquid surface. Nguyen et al. [55] carried out molecular-dynamics and long-wave continuum simulations of the capillary breakup of a nano-scale liquid metal ring on a solid surface. Gomes [32] computed the stability of a rotating toroidal gas bubble constrained between two concentric cylinders. The baseline situation, of a freely suspended torus in a quiescent medium, seems to have been studied only in Yao and Bowick [92]; they solved the Stokes flow during the contraction of the torus but did not investigate its capillary instability.

In this study we simulate the dynamics of a Newtonian torus suspended in a surrounding Newtonian liquid in three dimensions (3D). First we will study the linear growth of a sinusoidal disturbance on the torus and investigate the effect of the retraction and the axial curvature on the growth rate. Then we will examine the nonlinear instability and the final breakup into droplets. Finally the numerical results will be compared with the experiment.

3.2 Problem setup

Consider a Newtonian liquid torus of viscosity μ_t suspended in an immiscible Newtonian medium of viscosity μ_m. Initially the cross section of the torus is a circle of radius a_0, and the axis through the centre of the cross section is a circle of radius R_0. Hereafter, we refer to the curvatures due to R_0^{-1} and a_0^{-1} as the axial curvature and azimuthal curvature, respectively. Although non-varicose modes of instability are possible under external forcing, the experiments showed only varicose necking and breakup. Thus, we assume symmetry about the mid-plane of the torus, and only need to consider its top half. Furthermore, we can compute a half or a quarter of the top half for the growth of odd and even sinusoidal modes (Fig. 3.1). A sinusoidal perturbation of wavelength $\bar{l}_0$ is imposed on the torus at the start:

$$(r - R_0)^2 + z^2 = a_0^2 \left[1 + \delta_0 \cos\left(\frac{2\pi R_0}{\bar{l}_0} \right) \omega \right]^2, \qquad (3.1)$$

where r, z, and ω show the surface of the torus in cylindrical coordinates, $k = 2\pi R_0/\bar{l}_0$ is the number of waves along the circumference $2\pi R_0$, and δ_0 is the initial dimensionless amplitude. In presenting results, k will be called the *wave number*, though it differs from the usual sense of the word $(2\pi a_0/\bar{l}_0)$. We use the subscript 0 to indicate the initial condition. With contraction of the torus and growth of the disturbance, $a(t)$, $R(t)$, $\bar{l}(t)$ and $\delta(t)$ all change in time.

The subsequent fluid flow is governed by the Stokes equation; inertia and buoyancy are negligible in the experiment and will be neglected in the computations. For boundary conditions, we assume symmetry on the bottom and planar side walls of the domain of Fig. 3.1(a). The top wall is $11a_0$ above the top of the torus, on which we impose zero stresses. The outer cylindrical wall is at least $10a_0$ from the torus, and is solid with vanishing velocity. The outer boundaries are sufficiently removed from the torus that they do not affect the retraction and capillary instability on the latter. Toward the end of the chapter, when trying to match the experimental geometry of [57], we will bring the side wall closer to the torus.

Two dimensionless numbers quantify the physical problem: the torus-to-medium viscosity ratio $m = \mu_t/\mu_m$ and the initial aspect ratio of the torus $\beta = R_0/a_0$. The Cahn-Hilliard model introduces two more parameters, the Cahn number $Cn = \epsilon/a_0$ and a diffusion length scale $S = l_d/a_0$. We have used $S = 0.02$ and $Cn = 0.05$ throughout this chapter; this ensures the attainment of the sharp interface limit during torus retraction. The final breakup involves length scales shrinking to zero, and the finite thickness of the interface and the diffusion within will eventually manifest themselves. With $Cn = 0.05$, numerical experiments show that the pinch-off time increases by less than 5% when S decreases from 0.02 to 0.004. In presenting results, we use a_0 as the characteristic length and the capillary time $t_c = a_0\mu_t/\sigma$ as the characteristic time, σ being the interfacial tension. The wavelength l, however, will be scaled by the instantaneous circumference of the cross section of the torus $2\pi a$ to facilitate comparison with the straight-filament results. Note that t_c characterizes the capillary waves on the torus. Its retraction in the presence of a viscous external fluid is on the time scale $(R_0 - a_0)\mu_m/\sigma = t_c(\beta - 1)/m$.

3.3 Results: linear growth of capillary waves

Compared with the Rayleigh-Tomotika instability on a straight filament, several complications arise on the torus. First, due to the finite circumference of the torus, only a number of discrete wavelengths are possible for a given aspect ratio β. Second, the torus has an axial curvature (R^{-1}) which may affect the growth of the capillary wave. Finally, the contracting torus induces a flow in the surrounding fluid which may modify the capillary instability as well [52, 81]. Under the constraint of quantized wavelengths, the last two effects will be explored separately.

3.3.1 Quasi-static retraction: effect of axial curvature

By choosing a large initial aspect ratio β and a small viscosity ratio m, we can separate the time scales for the growth of the capillary wave and the retraction of the torus. In physical terms, this corresponds to a thin torus retracting slowly in a highly viscous bath. The speed of retraction dR/dt decreases in time. As an indication of its magnitude, $dR/dt = -0.0036$ at $R = 4$ for $m = 0.033$. For larger m, the retraction speed increases in proportion as expected. Such a quasi-static process is convenient in that we can probe the effect of the axial curvature on the linear instability of the torus while excluding the dynamic effect of the retraction-induced external flow. Furthermore, if we use a small enough initial perturbation and carry out the simulations on the time scale of torus retraction $t_c(\beta-1)/m$, we can record the linear growth rate at different axial curvatures and wavelengths. Thus a dispersion relation can in principle be generated in one simulation.

For one such torus with initial aspect ratio $\beta = 5.3$ and viscosity ratio $m = 0.033$, we impose two wave forms on it ($k = 2$). Different initial amplitudes ($\delta_0 = 0.005$ and 0.01) are tested, and $\ln(\delta/\delta_0)$ initially grows

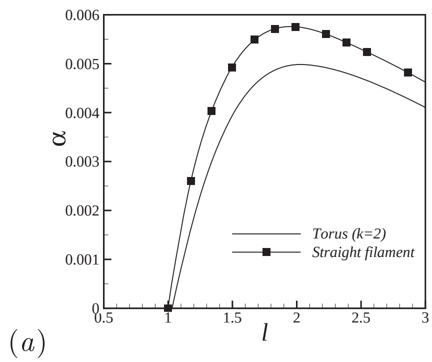

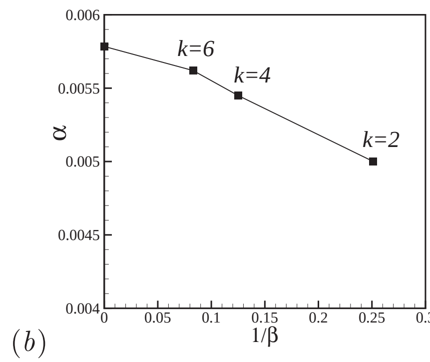

Figure 3.2: (a) Dispersion relation on a shrinking torus compared to that for a straight filament. The latter is computed by our diffuse-interface method and agrees with the Tomotika formula within 4%. The wavelength l and the growth rate α are made dimensionless by the instantaneous $2\pi a$ and t_c, respectively. (b) The linear growth rate decreases with the axial curvature for a prescribed dimensionless wave length $l_0 = 2$. The point at $1/\beta = 0$ corresponds to a straight filament.

linearly in time with a slope α that is independent of δ_0. This confirms that we are in the linear regime, with α being the growth rate. Over longer times (on the order of $t_c(\beta-1)/m \sim 100t_c$), the growth rate remains independent of δ_0 but starts to change in time. This is an effect of the torus retraction even though the instability is still in the linear regime. Since the wave number $k = 2$ is fixed, the wavelength shrinks with the retraction, not only in dimensional terms, but also relative to the thickening filament radius a. Thus, recording the growth rate as a function of the changing wavelength produces the dispersion relation in Fig. 3.2(a). The growth rate on the torus is some 15% below that on the straight filament, although the difference is expected to diminish for larger β. For $\beta \approx 10$, the difference narrows down to within 5%. In the limit of $R_0 \gg a_0$, of course, one recovers the growth rate on a straight circular cylinder. Therefore, *the axial curvature on the torus tends to hinder the growth of the capillary waves.* Note also that both the minimum wavelength for instability and the fastest growing wavelength have shifted slightly to longer waves from those for the straight filament.

The simulation above is not ideal in quantifying the effect of the axial curvature R^{-1} on the growth rate α since the former cannot be prescribed but continues to increase in time. For this purpose, we have conducted a series of simulations with tori of the same initial a_0, but different

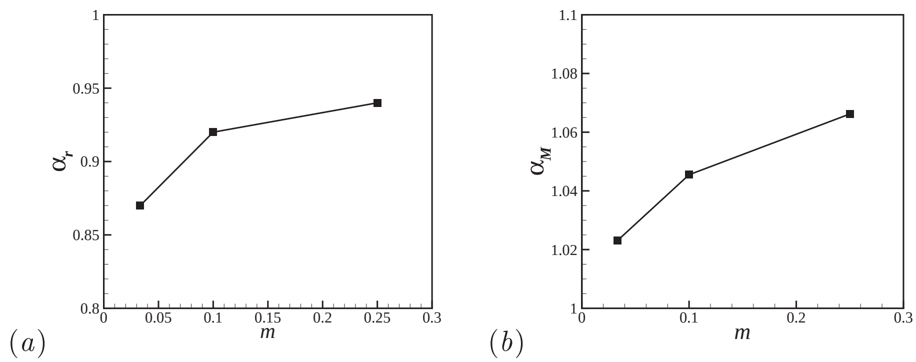

Figure 3.3: (*a*) Ratio of growth rates on a torus as a function of the viscosity ratio for a capillary wave of dimensionless wavelength $l = 2$. (*b*) Ratio of growth rates on a straight filament under uniform extensional flow, calculated from the theoretical result of [52].

initial aspect ratio β in proportion to the wave number k. Thus, these capillary waves have the same initial wavelength [in dimensionless form $l_0 = (2\pi R_0/k)/(2\pi a_0) = \beta/k = 2$], and differ only in the axial curvature R_0^{-1}. Fig. 3.2(b) plots the initial linear growth rate α as a function of $1/\beta = a_0 R_0^{-1}$, the non-dimensionalized axial curvature. It shows unequivocally that the instantaneous growth rate decreases with the axial curvature.

3.3.2 Faster retraction: effect of external flow

To examine the effect of the external flow field on capillary instability of the torus, we have gradually decreased the viscosity of the suspending fluid to produce faster retraction of the torus. Even on a straight filament, in the absence of the flow effect being examined, the ambient viscosity would have affected the growth rate. To remove this effect and isolate that of the retraction-induced external flow, we compute the ratio α_r between the growth rate on a retracting torus and that on a straight filament, the latter being calculated from the Tomotika formula using the same viscosities and the instantaneous filament diameter and wavelength of the torus. This ratio, as a function of m, demonstrates how the flow affects the growth of the instability. Note that the torus viscosity μ_t remains unchanged in this process; it gives a fixed time scale t_c against which the growth rate is measured. The faster retraction is then indicated by an increasing viscosity ratio m.

Fig. 3.3(a) plots the ratio of growth rates α_r against the viscosity ratio m for a dimensionless wavelength $l = 2$. With increasing m and hence increasing retraction speed, the growth rate ratio increases. This implies that the external flow induced by the torus retraction has the effect of *enhancing* the growth of instability. That α_r is below unity reflects the quasi-static effect of the axial curvature discussed in the preceding subsection.

It is interesting to compare this flow effect with that on a straight filament. [52] computed the effect of a uniform extensional flow on the capillary instability on a straight filament. The growth rate is written as the sum of two terms (see their Eq. 59). The first, due to the thinning of the filament and advective lengthening of the wavelength, had previously been computed by [81]. This effect is quasi-static in nature, and its counterpart on the torus has been included in the analysis of the last subsection. The second term, proportional to the strain rate G, explicitly accounts for the flow effect. From our torus retraction simulation, we extract a negative G from the rate of filament thickening, and then compute the two terms for the same wavelength $l = 2$. We take the ratio between the total growth rate and the first term, and plot it as a ratio of growth rates α_M in Fig. 3.3(b). This is not the same ratio as that in Fig. 3.3(a) since there is no axial curvature. Nevertheless, the qualitative trend is clear and confirms our observations on the retracting torus: the compression of a straight filament enhances the growth of capillary instability.

3.4 Results: nonlinear growth and breakup

The nonlinear instability and breakup of the torus must take place before the torus contracts onto itself. In this process, the quantized wavelength available and the initial amplitude of the perturbation are both important factors. Besides, the initial aspect ratio of the torus and the viscosity ratio are key parameters.

3.4.1 Fastest mode

On a retracting torus, with the wavelength and filament thickness changing continually, the *initially dominant mode* does not necessarily persist till breakup. In fact, the torus retraction should favor initially longer waves and this is illustrated in Fig. 3.4, with $\beta = 6.7$, $m = 0.033$ and $\delta_0 = 0.02$. Based on the dispersion relation for the torus, the linearly dominant wavelength is $l = 2.03$ and corresponds to a wave number $k = 3.3$. Thus, $k = 3$ or $k = 4$ should *initially* produce the fastest growth. Indeed, the two modes grow

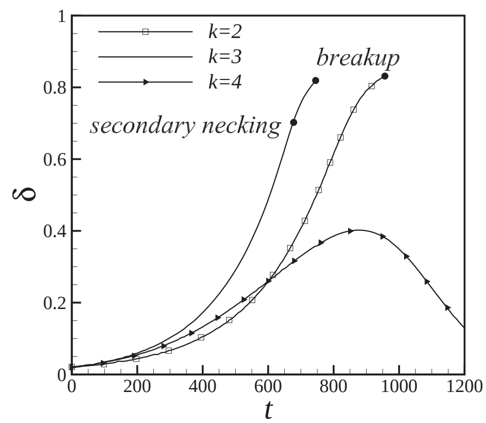

Figure 3.4: Nonlinear evolution of three modes of instability, with wave number $k = 2$, 3 and 4, for $\beta = 6.7$, $m = 0.033$ and initial amplitude $\delta_0 = 0.02$. δ is the instantaneous amplitude of the capillary waves. The curves for $k = 2$ and $k = 3$ end in breakup, with the onset of secondary necking also marked on the latter. The $k = 4$ mode ends in complete retraction.

at comparable rates at the beginning. But as the torus shrinks, the $k = 3$ mode maintains a high growth rate while the growth rate for $k = 4$ declines, leading eventually to retraction, not breakup. This can be rationalized by noting that for a retracting torus with a fixed wave number k, the wavelength gets shorter in time, in dimensional terms and especially relative to the growing thickness a. Thus the initially longer wave ($k = 3$) is favored over the shorter one ($k = 4$). The $k = 2$ mode grows more slowly but does lead to breakup. The breakup of the torus into droplets is depicted by snapshots in Fig. 3.5 for $k = 3$, starting from an initial perturbation of amplitude $\delta_0 = 0.02$. Primary necking proceeds at three points around the circumference of the torus until $t = 678$, when two secondary necks emerge around each primary neck. At $t = 748$ the torus breaks down into three primary drops and three satellite droplets. In time these all relax toward the spherical shape.

3.4.2 Pinch-off time versus retraction time

From the preceding discussion, it is clear that the breakup of the torus depends on the competition of two time scales: t_p needed for the neck to

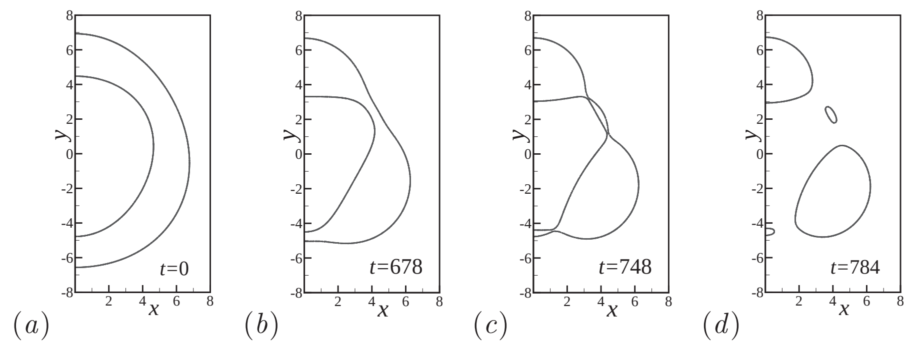

Figure 3.5: Snapshots of the evolving interface on the mid-plane of the torus for $\beta = 6.7$, $m = 0.033$ and $\delta_0 = 0.02$. The interface is given by the level set of $\phi = 0$.

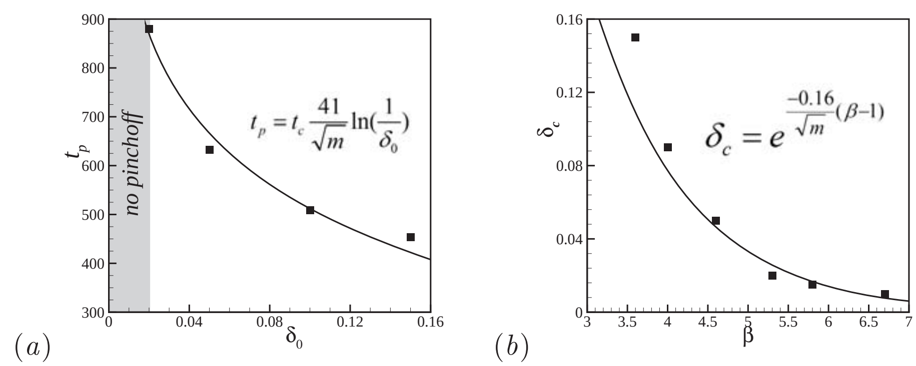

Figure 3.6: (a) The pinch-off time decreases with increasing initial amplitude of disturbance. $\beta = 5.3$, $m = 0.033$, $k = 2$. The solid curve is the best fitting by Eq. (3.2). (b) The critical initial amplitude δ_c decreases with the initial aspect ratio β. The solid curve is the best fitting by Eq. (3.3).

pinch off, and t_s needed for the torus to shrink onto itself. This competition can be affected by multiple factors. For example, the $k = 4$ mode of Fig. 3.4 can survive till breakup if the initial perturbation has a sufficiently large amplitude; δ_0 defines t_p. Besides, the breakup depends on the initial aspect ratio β and the viscosity ratio m, each having a role in t_s. These three factors will be examined in turn.

Fig. 3.6(a) demonstrates the dependence of the pinch-off time t_p on the

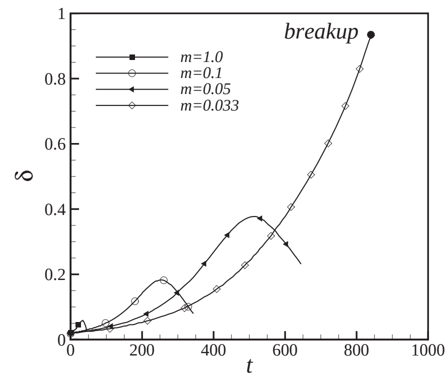

Figure 3.7: Effect of the viscosity ratio on the growth of disturbance. $\beta = 5.3$, $\delta_0 = 0.02$ and $k = 2$.

initial amplitude δ_0 for $\beta = 5.3$, $m = 0.033$ and $k = 2$, which is the initially dominant mode. If δ_0 is below a critical value $\delta_c \approx 0.02$, no breakup occurs. For $\delta_0 > \delta_c$, the torus breaks up into two principal drops and two satellite droplets, and t_p decreases with increasing δ_0 as expected. Besides, the faster the breakup, the larger the satellite droplets. The critical amplitude δ_c decreases with increasing initial aspect ratio β, as shown in Fig. 3.6(b). The thinner, longer torus offers a longer t_s within which breakup can take place. In the β range shown, $k = 2$ persists till breakup from all $\delta_0 > \delta_c$; no other modes emerge from noise to overtake the imposed $k = 2$ mode.

The viscosity ratio $m = \mu_t/\mu_m$ is another parameter that modulates the competition between pinch-off and retraction. Our results show that the torus retraction is more influenced by the matrix viscosity μ_m while the necking and pinch-off more by the torus viscosity μ_t. As m increases from 0.033 to 0.05 and 0.1, the critical amplitude δ_c increases from 0.02 to 0.03 and 0.07. For $m = 0.5$ even $\delta_0 = 0.18$ is unable to break down the relatively viscous torus before it contracts into a single drop, often entrapping a droplet of the ambient fluid in the centre [97].

Fig. 3.7 illustrates the effect of m on the growth of an initial disturbance with $k = 2$, which is the initially dominant mode for all the m values considered here. Since time is scaled by $t_c = a_0\mu_t/\sigma$, using the torus viscosity, increasing m can be conveniently thought of as due to a decreasing μ_m. As μ_m decreases, the initial growth rate of the capillary wave increases. However, the retraction of the torus becomes faster as well. Numerical experiments show that the latter has the upper hand. Thus, for lower μ_m, δ reaches a maximum quickly and then declines, due to the thickening of the torus and the effective shortening of the wavelength. It is for the largest matrix viscosity, at $m = 0.033$, that the slow retraction offers the capillary disturbance sufficient time to grow till breakup, despite the slower linear growth rate.

The competition between time scales can be represented by scaling arguments. As noted earlier, the shrinkage time $t_s \sim t_c(\beta - 1)/m$. The pinch-off time can be taken as that required for the disturbance to grow from the non-dimensionalized initial amplitude δ_0 to 1: $t_p = -\ln \delta_0/\alpha_m$, where the fastest growth rate α_m can be estimated from the Tomotika solution: $\alpha_m \sim \sqrt{m}/t_c$ [18]. Therefore, we can write

$$t_p = t_c \frac{c_1}{\sqrt{m}} \ln\left(\frac{1}{\delta_0}\right), \tag{3.2}$$

and $c_1 = 40.6$ gives a reasonably good fitting to the numerical data in Fig. 3.6(a). Furthermore, equating this t_p with the shrinkage time t_s gives us the critical initial amplitude for breakup:

$$\delta_c = \exp\left(-c_2 \frac{\beta - 1}{\sqrt{m}}\right), \tag{3.3}$$

which fits the data in Fig. 3.6(b) well with $c_2 = 0.16$. Given that much of the necking and pinch-off is nonlinear, these linearly based scaling relationships work remarkably well.

3.5 Comparison with experiment

As far as we know, the only prior experiment on the breakup of a freely suspended torus is that of Pairam and Fernandez-Nieves [57]. With Newtonian glycerol tori in a Newtonian oil bath, these authors reported that thick tori shrink to one droplet while thin ones break down into a number of droplets through Rayleigh-Tomotika instability. We match the liquid viscosities and flow geometry in the experiment, where the torus is confined in a cylindrical drum, with the top and side walls being some $6a$ away from the outer edge of the torus. Our numerical experimentation shows that this confinement is essential for slowing down the torus retraction and allowing breakup. Still two uncertainties complicate a direct comparison. The first is the initial amplitude of perturbation δ_0. In the experiment, the torus is generated by releasing a glycerine jet into silicone oil while the drum rotates. There is

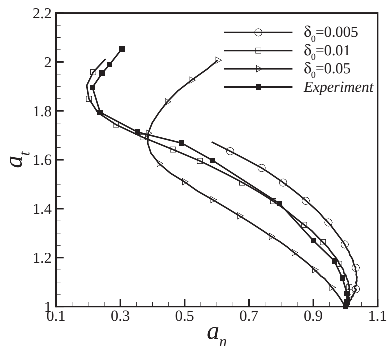

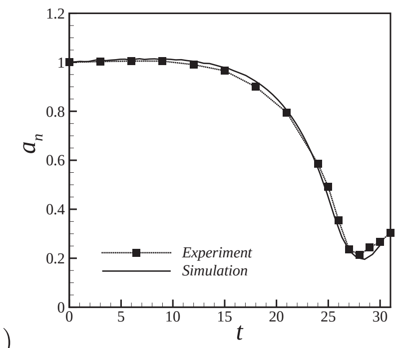

Figure 3.8: (a) Determining the initial amplitude of perturbation δ_0 from the variation of the thickest radius a_t versus the thinnest radius a_n on the torus. Both radii are normalized by the initial value a_0. (b) Determining the interfacial tension σ from the temporal variation of a_n. $\beta = 5.3$, $k = 2$ and $m = 0.033$.

a complex flow history, and it is not obvious how to gauge the magnitude of the initial perturbation. The second is the interfacial tension σ in the experiment. It was not reported and cannot be made available to us. We determine δ_0 and σ first by fitting the experimental data.

First note that the capillary time t_c is the only time-scale of the problem, and the only role of σ is to lengthen or compress t_c. Thus, in Fig. 3.8(a) we plot the radius a_t of the thickest part of the torus against the thinnest radius a_n at the neck. Such a curve should be independent of t_c. Among numerical results starting from different δ_0 values, $\delta_0 = 0.01$ agrees very closely with the experiment. So we take $\delta_0 = 0.01$ to be the initial amplitude for this case. Now plotting the temporal variation of the neck radius in Fig. 3.8(b) gives us a fitting of $\sigma = 31.8$ mN/m, which is within the 5 percent of the handbook values [63].

With the δ_0 and σ values determined, we compare the number of primary drops N between the simulation and the experiment for a range of torus aspect ratio β (Fig. 3.9). All the simulations have started with the fastest linear mode for the β value. The results agree with the experiment except for $\beta = 4$, where the simulation predicts complete retraction, while the experiment reported $N = 1$, breakup at a single primary neck for the $k = 1$ mode. We cannot explain this at present; possibly this experiment had a different δ_0 from that fitted in Fig. 3.8(a) for $\beta = 5.3$. Numerical experimentation indicates that $\delta_0 = 0.02$ would lead to breakup at a single

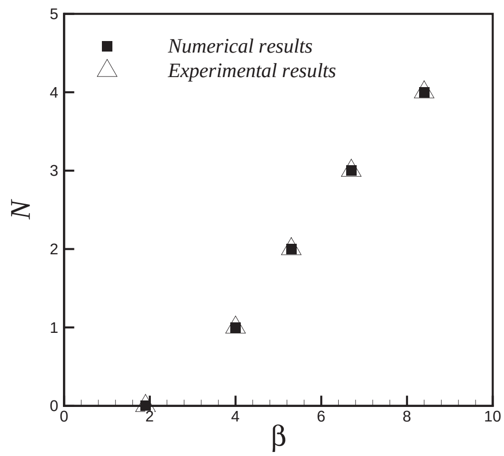

Figure 3.9: Comparison between the predicted and observed number of primary drops after breakup, for tori with five initial aspect ratios. $m = 0.033$ and $\delta_0 = 0.01$. $N = 0$ and 1 refer to, respectively, complete retraction with no breakup and breakup at a single primary neck.

neck. In all the cases leading to breakup, N corresponds to the fastest linear mode. Even though the wavelength and filament thickness both change during the retraction, we have never seen the linearly dominant mode yielding to a nascent mode in the nonlinear stage. This reflects the fact that there is a limited time window for growth and it is too short for another mode to emerge spontaneously from random noise.

3.6 Summary and conclusions

Capillary instability of a Newtonian liquid torus is studied by imposing a sinusoidal disturbance on an initially stationary torus in quiescent surrounding Newtonian liquid. The main findings of this study are

(a) If the initial disturbance has sufficiently small amplitude, the capillary instability initially grows linearly, at a growth rate independent of the amplitude of the disturbance.

(b) The geometry of the torus can affect the capillary instability through its axial curvature and the external flow field.

(c) Effect of axial curvature on the disturbance growth is studied by choosing a very viscous surrounding liquid and hence producing very slow retraction. A dispersion relation is constructed for the torus by looking at the growth rate of the disturbance during the shrinkage. It is shown that axial curvature decreases the growth rate of the disturbance compared to straight filament.

(d) Effect of the external flow field on capillary instability of the torus is examined by gradually decreasing the viscosity of the surrounding fluid to produce faster retraction of the torus. By finding the ratio of the growth rate of a certain wavelength on a torus to its counterpart on a straight filament, it is shown that shrinkage enhances the capillary instability. This is further confirmed by comparing the flow induced term and quasi-static term in the equation proposed by [52] for the flow effects in a straight filament.

(e) The final shape of torus is a result of competition between two time-scales called shrinkage and pinch-off timescale. Shrinkage can be scaled as $t_s \sim t_c(\beta - 1)/m$ which shows that it is inversely proportional to viscosity ratio and is proportional to aspect ratio of the torus as well as capillary timescale. The pinch-off time depends on the wavelength. If we choose the fastest one and assume that the growth rate is almost equal to the initial growth rate during the retraction. The following scaling can be proposed for the pinch-off time: $t_p \sim \frac{t_c}{\sqrt{m}} \ln\left(\frac{1}{\delta_0}\right)$. Competition of these two time-scales determines the final shape of the torus.

Chapter 4

Wicking Flow through Microchannels

4.1 Introduction

As mentioned in Chapter 1, capillary force is a key mechanism to move flow inside narrow channels of porous media and microfluidic devices that typically consist of complex geometric features. Dynamics of interface is dependent on the geometry of the conduit, and it is usually ignored in previous studies of wicking flow, which is typically one-dimensional. There are theoretical and numerical difficulties in computing wicking flows through complex geometries. These include the lack of a good model for the moving contact line, the need to capture dynamically a moving and deforming interface, morphological singularities in coalescence and rupture of interfaces, and the complex flow geometries in practically interesting problems. The first three are generic to simulation of interfacial flows. The last, on geometry, is especially pertinent to flow in porous medium. The geometric features of a pore include changes in the cross-sectional area between wide pore chambers and narrow pore throats, branching and intersection of pores, and the appearance of sharp edges and corners on which a gas-liquid interface can be pinned.

The classic work on wicking flows is that of Lucas [49] and Washburn [85], who computed capillary rise in straight tubes. This solution is notable for its simplicity. Dynamics of the meniscus is completely ignored. In its place, a static interfacial shape is assumed such that the interface merely supplies a constant suction pressure. In addition, the flow in the tube is taken to be fully developed Poiseuille flow. Now the capillary rise can be computed by balancing the capillary pressure against the viscous friction. Later work has sought to include inertia, dynamic contact angle and entry effects [8, 23, 42, 70, 98]. More recently, tubes of non-circular cross sections have also been considered [35].

Of more relevance to our work are generalizations of the Lucas-Washburn solution to tubes and channels of gradually varying cross sections. Using the lubrication approximation, *one-dimensional* (1D) solutions have been obtained for sinusoidal tubes [68, 73], sinusoidal tubes with tortuosity [60] and tubes and channels with convergent, divergent and power-law cross sections [66]. Liou *et al.* [47] extended the previous solutions to 2D axisymmetric flows by using approximate velocity profiles. This allowed them to include inertia as well as viscous stresses that vary with the cross-sectional area.

The only numerical study of wicking flow inside tubes with convergent-divergent cross section is done by Erickson *et al.* [25] They have computed the 2D axisymmetric flow inside tubes by finite elements, but excluded the hydrodynamics of the interface as in the analytical studies mentioned above. By assuming a spherical shape of the meniscus, they update its position from the liquid volume flow rate. The capillary pressure is introduced by the Young-Laplace equation along with a dynamic contact angle. Perhaps to minimize the disturbance to the meniscus and to make the spherical shape a more accurate approximation, they have used very long tubes with exceedingly mild contractions and expansions, with a contraction/expansion angle of 0.5°. A surprising prediction is that if the total lengths of the wider and narrower portions of the tube are fixed, the time for the meniscus to pass through the tube is independent of the number of the contraction/expansion cycles along the tube's length.

To summarize this brief review of the literature, previous studies have ignored the hydrodynamics of the meniscus. The motion of the contact line is unaccounted for, and the meniscus shape is always prescribed to be spherical. Little can be found in the literature that deals with the detailed morphological changes of the meniscus during its motion through complex geometries. As such, their applicability to two-phase transport in porous media is quite limited. For one, pinning of the interfaces on sharp corners of the pore is responsible for pore blockage and, if external pressure is applied, eventual capillary breakthrough [22, 48]. Competition among interconnected pores will depend on the dynamics of the interfaces in complex geometries, including rupture and coalescence as the meniscus negotiates bifurcations and junctions. Finally, the wettability of porous medium is often manipulated to enhance two-phase transport [58]. The underlying mechanism has to be sought from the hydrodynamics of the interface. In this context, a fundamental understanding of interfacial dynamics during wicking through complex geometry is essential. In view of the various difficulties mentioned above, however, a rigorous study of the dynamics of the meniscus based on hydrodynamic principles has yet to be done.

This chapter presents an initial effort toward addressing these issues. We

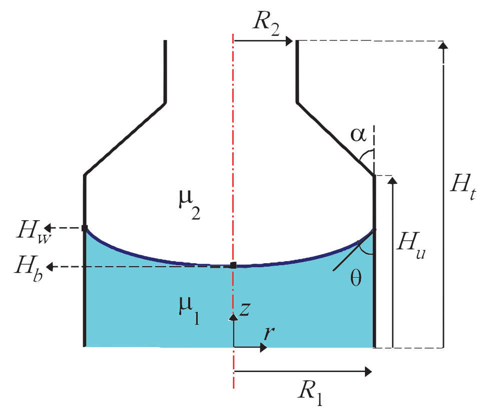

Figure 4.1: Schematic of the flow geometry for wicking into a capillary tube with contraction.

examine the two quintessential geometric features of a porous medium: the areal changes between pore throats and chambers and the branching of flow conduits. Specifically, we simulate the wicking flow in axisymmetric tubes with non-uniform cross sections and 2D planar channels that bifurcate into two branches. Using a Cahn-Hillard description of the contact line dynamics allows us to capture the moving interface and its morphological changes accurately and naturally, including pinning at sharp corners and otherwise singular interfacial breakup at bifurcations. We show that the meniscus undergoes complex deformations through contractions and expansions, with contact line pinning at protruding corners and turning of the interface at concave corners. Capillary competition between bifurcating channels may suppress wicking in the wider branch in favor of the narrower one. Manipulating the wettability in the branches can even produce flow reversal.

4.2 Problem setup

Wicking is significant in small capillary tubes and pores, and the resulting Reynolds and Bond numbers are typically much below unity. Therefore, we will neglect inertia and gravity throughout this work, and highlight the roles of capillarity and viscosity. The hydrodynamics is governed by the continuity equation and a modified Stokes equation.

The computational domain is illustrated in Fig. 4.1. Natural boundary conditions are employed at the inlet and the outlet. In addition, the pressure is set to be equal between the inlet and the outlet such that the motion of the liquid column is driven entirely by wicking, i.e. by the capillary pressure generated by the meniscus.

The wicking flow consists in a column of hydrophilic fluid of viscosity μ_1 displacing a hydrophobic one of viscosity μ_2 (Fig. 4.1). The geometrical parameters include the contraction or expansion angle α, the total length H_t, length of the upstream section H_u, and the larger and smaller tube radii R_1 and R_2. In Fig. 4.1, H_b denotes the position of the center of the meniscus, hereafter called its *base point*. H_w marks the position of the contact line on the wall, hereafter called the *wall point* of the meniscus. Initially, there is no flow and the liquid column is at $H_w = H_0$. Later, both H_w and H_b vary in time as the wicking proceeds. In this dynamic process, the interface shape is determined by the viscous and capillary forces, and is in general not spherical. However, it will prove convenient to use an *effective curvature* κ, defined for a spherical surface, in discussing the evolution of the interface. From the height of the meniscus $\delta_m = H_w - H_b$ and the local tube radius R, we can calculate the radius of the spherical surface that passes through the wall and base points of the meniscus: $\rho_s = \frac{R^2+\delta_m^2}{2\delta_m}$, from which we can define:

$$\kappa = \frac{2\delta_m}{R^2 + \delta_m^2}. \tag{4.1}$$

Note that κ is an overall indication of the meniscus curvature, and does not reflect the local deformation of the interface. It varies along the axis in an expansion or contraction as R does. In presenting results in dimensionless form, we scale length by R_1, curvature by R_1^{-1}, velocity by σ/μ_1 and time by $\mu_1 R_1/\sigma$. Throughout this study we have set $R_2/R_1 = 0.5$ and $H_t/R_1 = 20$ except in Fig. 4.10 where $H_t/R_1 = 21$.

The physical parameters of the problem can be combined into two dimensionless parameters: the static contact angle θ and the viscosity ratio $m = \mu_2/\mu_1$. Unless noted otherwise, m is set to 0.02 to represent the viscosity ratio between air and water at room temperature.

4.2.1 Choice of Cahn-Hilliard parameters

As discussed in Chapter 2, the contact line velocity is very small for the considered wicking flow so we assume fast wall relaxation and set Π equal to zero. Therefore, the diffuse-interface model introduces two additional lengths [96]: the interfacial thickness ϵ and a *diffusion length* $l_d = \gamma^{1/2}(\mu_1\mu_2)^{1/4}$. They produce two dimensionless parameters: the Cahn number $Cn = \epsilon/R_1$ and $S = l_d/R_1$. ϵ or the Cahn number Cn should be sufficiently small so that the numerical results no longer depend on it; this is known as the sharp interface limit. To ensure that the sharp-interface limit for moving contact

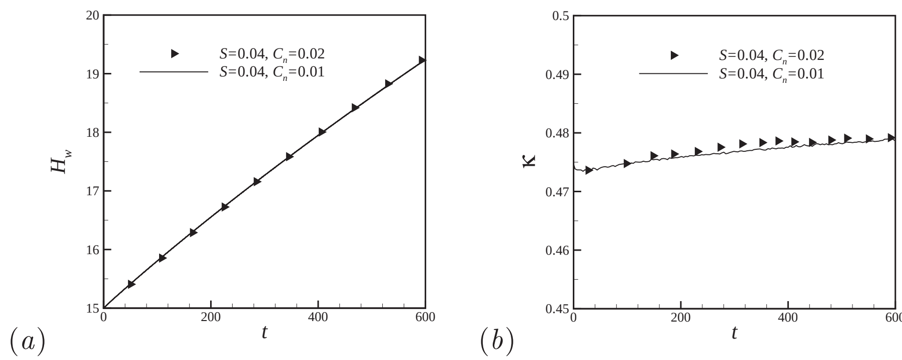

Figure 4.2: Sharp-interface limit for computing capillary rise. (a) Contact line motion indicated by the rise of H_w in time for two Cahn numbers $Cn = 0.01$ and 0.02. (b) Variation of the effective meniscus curvature κ with time for the same two Cn values. $S = 0.04$, $\theta = 60°$, the tube radius $R = 1$, total length $H_t = 20$ and the initial column height $H_0 = 15$.

lines is achieved, we use the criterion of Yue *et al.* [96]: ($Cn \approx 4S$). In our wicking problem, the criterion turns out to be more stringent than that of Yue et al. [96]. We tested a range of Cn values for $S = 0.04$, and found the results to be essentially independent of Cn once it is below 0.02. Fig. 4.2 shows that the contact line motion and the meniscus shape agree closely between $Cn = 0.02$ and $Cn = 0.01$. Thus, the sharp-interface limit is achieved by using $Cn = 0.02$ in this case.

As discussed in Chapter 2, the diffusion length l_d or the parameter S, should be chosen to match a single experimental measurement. In this section, we examine these issues in the simple geometry of imbibition and drainage in a straight capillary tube. Our aim is twofold: to select a suitable value for S, and to validate the numerical results for a straight circular tube against the Lucas-Washburn formula [49, 85].

In the capillary rise problem, the Lucas-Washburn formula [49, 85]

$$H(t) = \sqrt{H_0^2 + \frac{\sigma R \cos\theta (t - t_0)}{2\mu}} \tag{4.2}$$

is widely accepted as an accurate representation of the interfacial movement, as long as the liquid column is long enough such that the "end effect" is negligible and the flow can be approximated by the Poiseuille flow. Here, R is the tube radius, μ is the viscosity of the liquid and that of the gas is

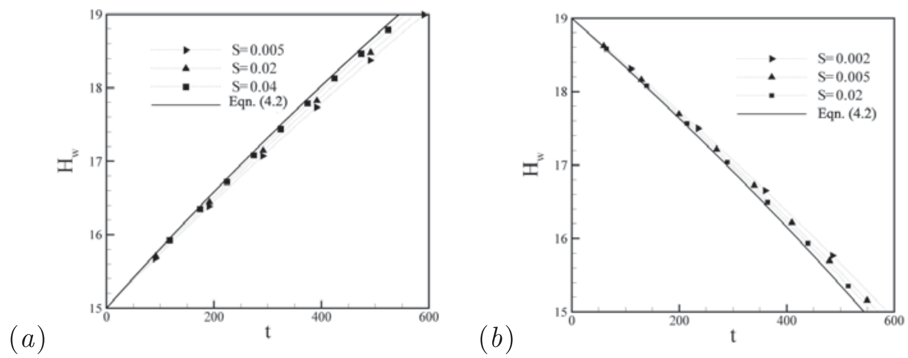

Figure 4.3: Comparison between the diffuse-interface simulation and the analytical Lucas-Washburn formula at different S values. (a) Imbibition with $\theta = 60°$, Cn=0.01, $m = 0.02$ and $H_0 = 15$. (b) Drainage with $\theta = 120°$, Cn=0.01, and $H_0 = 19$. Now the less viscous component is wetting, and the non-wetting-to-wetting viscosity ratio $m = 50$.

neglected.

Fig. 4.3 compares our diffuse-interface calculation of capillary imbibition and drainage at several S values with the Lucas-Washburn formula. A few observations can be made. First, in both imbibition and drainage, the numerical result approaches the analytical formula as S increases. While the analytical solution neglects the dynamics at the meniscus and the contact line completely, the Cahn-Hilliard model includes a friction at the contact line in terms of an additional dissipation [97]. As the diffusion length or S increases, the effective slippage at the contact line increases, thus reducing the influence of this friction. For $S = 0.04$, the effective curvature of the interface is 5% lower than that expected of a spherical surface. This is due to the flow effects at the meniscus that the Lucas-Washburn formula disregards.

Second, the contact line speed is insensitive to S. With a tenfold change in S, the contact line speed changes by some 6%. This forms an interesting contrast to the situation studied by Yue *et al.* [96], where in shear flows the meniscus shape or interface inclination is highly sensitive to S. This can be rationalized by the fact that the contact line speed is determined by equating the viscous dissipation to the surface energy gained by wetting or dewetting. Thus, insofar as most of the dissipation occurs in the bulk of the column, the effect of S is mild. In shear flows, in contrast, the contact line speed is prescribed, and the amount of Cahn-Hilliard diffusion affects the shape of the interface greatly.

Third, the same S produces larger deviation from the Lucas-Washburn formula for imbibition than for drainage. This reflects the fact that the viscosity of the displacing and the displaced components contributes to the contact line motion differently. But this asymmetry is not reflected by the definition of S used here. Finally, there is an upper limit to reasonable S values. Using too large a diffusion length l_d exaggerates the area that is directly affected by the contact line. Our numerical experiment shows that for $S = 0.15$, for example, the overall features of the flow are distorted by the interfacial diffusion and the solution becomes very inaccurate. In typical flow situations, the slip length is orders of magnitude smaller than the macroscopic length scale [20, 94].

To sum up this section, we have demonstrated how the sharp-interface limit can be achieved by using a small enough Cn and how S can be selected by comparing with the Lucas-Washburn formula. Most of the results to be presented are for $S = 0.04$ and $Cn = 0.01$. For the wicking through multiple contraction-expansion combinations (Fig. 4.10), we have used $Cn = 0.02$. To better resolve contact line pinning and turning at corners (e.g., Figs. 4.4 and 4.7), we have used a smaller $Cn = 0.005$.

4.3 Wicking in a tube with contraction or expansion

We consider the wicking flow of a liquid column into an axisymmetric tube, with a contraction as shown in Fig. 4.1 or with an expansion. The goal is to elucidate the detailed hydrodynamics of the moving interface, in particular how the contact line negotiates concave and convex corners. Also of interest is the passage time as a function of the flow geometry, with a single contraction-expansion combination or multiple cycles of it.

4.3.1 Contraction

Fig. 4.4 illustrates the wicking of a liquid through a 2:1 contraction at contraction angle $\alpha = 45°$. The wall is hydrophilic to the liquid, with a wetting angle $\theta = 60°$. The evolution of the interface is punctuated by several critical points marked on the $H_b \sim H_w$ and $\kappa \sim H_w$ curves as well as by the insets. In the first stage of the process ($H_w < H_u$), the meniscus moves with a constant shape within the wide tube before it reaches the contraction.

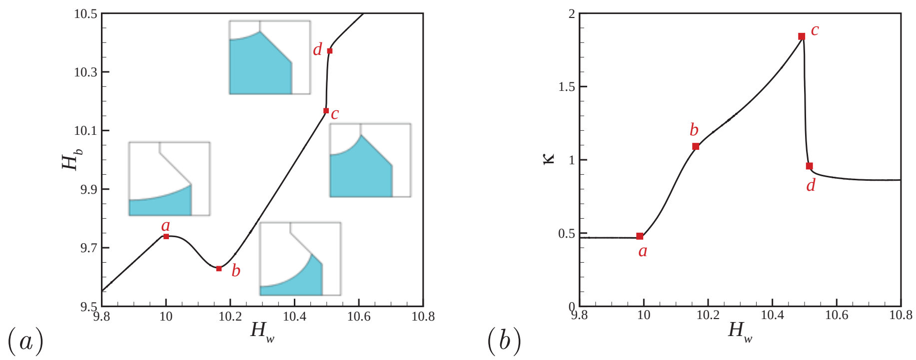

Figure 4.4: Meniscus movement through a contraction with $\alpha = 45°$ represented by (a) the variation of the base point with the wall point, and (b) the effective curvature defined in Eq. (4.1). $\theta = 60°$, $Cn = 0.005$ and $H_u = 10$. In (a) the insets correspond to the four points marked by squares on the curve. In (b) the dashed line indicates the curvature expected of a quasi-static spherical meniscus.

The base point and wall point advance at equal speed and the trajectory in Fig. 4.4(a) is a straight line with slope 1. The meniscus is not spherical, however. Viscous forces distort it so that the constant effective curvature κ is 6% below that expected of a spherical meniscus at equilibrium in the upstream portion of the tube.

As the contact line reaches the corner at the beginning of the contraction, marked by point a in the plot, a new behavior sets in. First, the contact line quickly moves past the concave corner. Once it is on the inclined wall of the contraction, the interface must rotate by α to maintain the same contact angle θ with the wall. This rotation first occurs locally at the contact line, elevating the local curvature. Then the interfacial distortion propagates toward the center by interfacial tension, causing the central portion of the meniscus to pull back upstream. This process is reflected in Fig. 4.4(a) by the downturn of the trajectory and the sharp upturn of κ in Fig. 4.4(b). The interfacial adjustment is completed by point b, when the base point of the interface is at a minimum. During this highly dynamic transition, κ falls far below what one would expect by assuming a quasi-static spherical meniscus.

After point b, the base point moves forward again, and at a higher speed than the wall point because R is shrinking and the interface is continuously becoming more curved. Hence the continued increase in κ. The next mile-post is when the contact line reaches the convex corner marking the end of the contraction (point c). The contact line is *pinned* at the corner [37] while the base point continues to move forward. Thus the interface rotates toward the downstream as if hinged at the corner, and in the mean time straightens with a steep decline in κ. The pinning ends when the angle between the interface and an extension of the downstream wall reaches the contact angle θ, in accordance with Gibbs' pinning criterion, and the meniscus as a whole moves into the narrow channel. This moment is marked by d in Fig. 4.4. The effective curvature κ settles into a steady value roughly 14% below that for a perfectly spherical meniscus at equilibrium.

4.3.2 Regularization of corner singularity

The turning of the interface at the concave corner (point a) deserves a closer examination. The case illustrated in Fig. 4.4 has a relatively mild contraction with $\alpha < \theta$. Thus, as the contact line advances from the corner onto the ramp, the interface rotates locally by α to form a tight curve, which is subsequently smoothed out over the rest of the interface. Now imagine a stronger contraction with $\alpha > \theta$. If the interface rotates by α at the corner, it would have to penetrate the wall upstream. Hence, a concave corner with a contraction angle larger than the wetting angle appears to present a singularity to the contact line.

This singularity is not real, of course. It arises because the foregoing argument is made in the classical sharp-interface framework, with the interface being viewed as a mathematical surface of zero thickness. This is a good representation of real interfaces as long as the length scale of interest is much larger than the interfacial thickness. At a concave corner of sufficiently large α, the turning of the interface entails intersection with the solid wall, which in reality would invoke physics on the molecular length scale. Little surprise that an apparent singularity should appear. In fact, a strict implementation of the sharp-interface model would encounter difficulty even for a contact line moving on a *flat* substrate [61, 62].

This is where the diffuse-interface model presents a distinct advantage. By preserving the reality that interfaces are diffuse mixing layers rather than discontinuities, the model circumvents the traps of singularity on flat substrate as well as at corners. On a flat substrate, Cahn-Hilliard diffusion allows a contact line to move and predicts a dynamic contact angle [94, 96]. Inside a concave corner, diffusion allows the interface to turn a large α in a natural manner as demonstrated in Fig. 4.5.

We have to point out that the diffuse-interface model introduces a local length scale ϵ, the interfacial thickness. If the physical process being

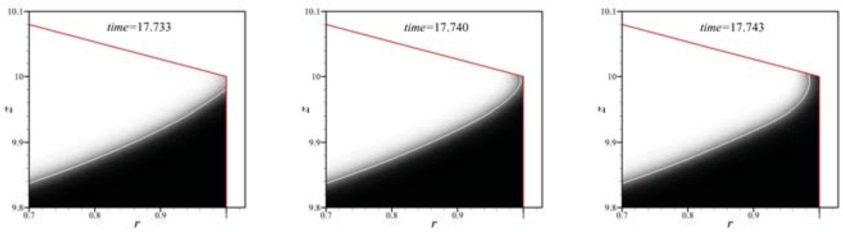

Figure 4.5: Gray-scale contours of ϕ depicting the interface traversing a concave corner through Cahn-Hilliard diffusion. The light line indicates the contour of $\phi = 0$. The contraction angle $\alpha = 75°$ is greater than the wetting angle $\theta = 60°$. $H_u = 10$ and initially the meniscus is at $H_0 = 9.8$.

studied involves a length scale that shrinks indefinitely, as occurs here in Fig. 4.5 and during interfacial pinch-off or rupture [29, 95], the finite-ϵ effect manifests itself eventually, and is intrinsic to the diffuse-interface formalism. Therefore, the negotiation of the corner in Fig. 4.5 occurs more slowly with decreasing ϵ. The question of choosing suitable Cahn-Hilliard parameters has been discussed elsewhere [94]. For the current problem, the diffuse-interface model regularizes the singularity at the corner and captures the qualitative features of the process, but cannot foretell what ϵ value would predict reality quantitatively.

4.3.3 Expansion

Wicking through an expansion, schematically depicted in Fig. 4.6, differs from wicking through a contraction in that the contact line first encounters a convex corner, and then a concave one. The process is illustrated in Fig. 4.7. When the meniscus is entirely inside the narrower channel upstream, H_w and H_b advance with the same speed. As the contact line reaches the corner at the start of the expansion (point a), it is pinned temporarily according to Gibbs' pinning criterion [37]. Meanwhile the base point moves forward very quickly until point b, when the interface reaches an angle of $\theta + \alpha = 85°$ with respect to the upstream wall. It depins from the corner, and the entire meniscus advances through the expansion. This corresponds to the segment between points b and c. At point c, the meniscus reaches the end of the expansion with the contact line at the concave corner. As the wall rotates counterclockwise by α at this corner, so must the interface before it could march downstream onto the straight portion of the tube. This causes a large local curvature of the interface, which propagates toward the center, causing

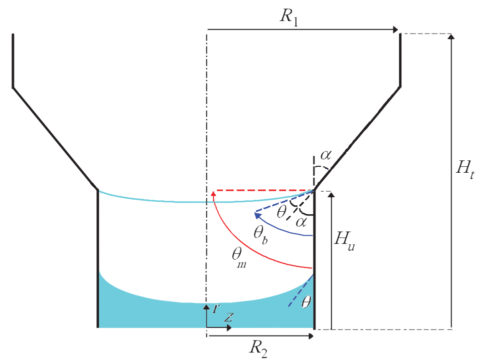

Figure 4.6: Schematic of an expansion illustrating the pinning criterion. $\theta_b = \alpha + \theta$ is the breakthrough angle, and $\theta_m = 90°$ is the maximum angle that the interface may reach at the corner.

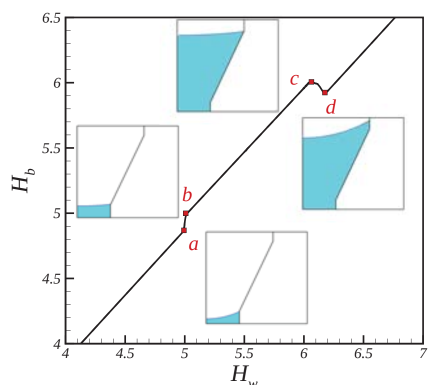

Figure 4.7: Wicking through an expansion with $\alpha = 25°$, $\theta = 60°$, $Cn = 0.005$ and $H_u = 5$. The insets correspond to the four points a–d on the curve.

the base point of the meniscus to retreat, as illustrated by the decline of H_b beyond point c. Once this interfacial adjustment is completed at point d, the entire meniscus moves down the wider straight channel, again with the base point and wall point advancing at the same speed.

Naturally one contrasts the above process with wicking through a contraction (Fig. 4.4). The behavior at the concave corner at the end of the expansion, between points c and d in Fig. 4.7, is essentially the same as

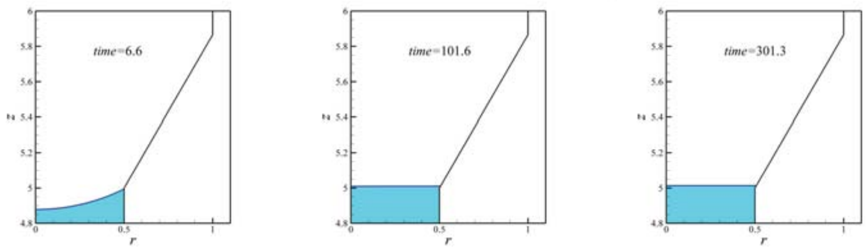

Figure 4.8: Permanent pinning of the interface at the entrance to an expansion with $\alpha = 30°$. $\theta = 60°$, $C_n = 0.005$, $H_u = 5$ and $H_0 = 4.9$.

appears at the start of the contraction, from a to b in Fig. 4.4. If the expansion is too abrupt, with $\alpha > \theta$, the corner would present a singularity to a sharp-interface model but not to our Cahn-Hilliard model. On the other hand, the convex corner at the start of the expansion, point a in Fig. 4.7, differs fundamentally from its counterpart, point c in Fig. 4.4; here it has the potential of *permanently* pinning the interface. This would happen if the expansion is abrupt enough such that the required breakthrough angle $\theta_b = \theta + \alpha$ is beyond the maximum achievable $\theta_m = 90°$:

$$\alpha + \theta \geq 90°. \tag{4.3}$$

Such a situation is illustrated by the snapshots in Fig. 4.8 for $\theta = 60°$ and $\alpha = 30°$. After the contact line gets pinned at $t = 6.6$, the interfacial tension acts to move the rest of the interface forward so as to minimize the interfacial area. This continues till $t = 101.6$, when the meniscus becomes a flat surface and can move no further. At this point, the angle between the interface and the upstream wall is $\theta_m = 90°$, barely equal to the breakthrough angle θ_b. The contact line cannot depin and the flow is arrested permanently. Thus, the geometric constraint of Eq. (4.3), based on the Gibbs pinning condition [37], specifies a degree of expansion beyond which a hydrophilic fluid cannot enter. This may be contrasted with the convex corner at the end of the contraction (point d of Fig. 4.4). As long as the fluid is hydrophilic ($\theta < 90°$), the contact line always depins before the meniscus becomes flat at 90° angle with the downstream wall.

4.3.4 Penetration time

The speed of wicking and the time required to penetrate a given depth are of practical significance in various applications [10, 54, 60], and have been

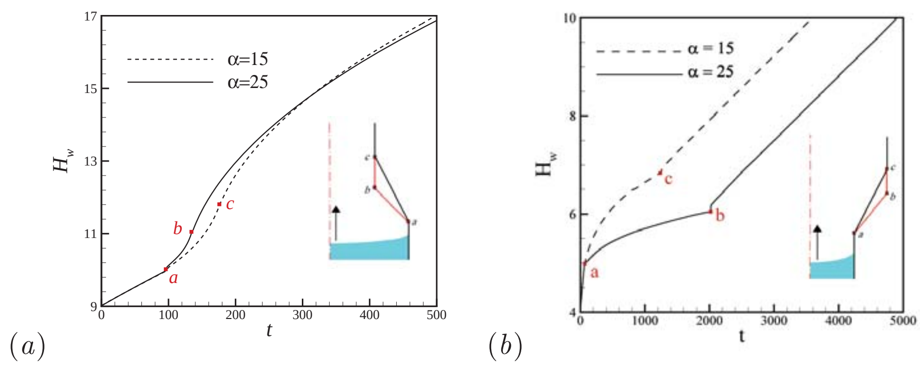

Figure 4.9: (a) Comparison of wicking speed through 2:1 contractions at two contraction angles $\alpha = 15°$ and $25°$. The inset illustrates the flow geometry. $H_u = 10$, $H_0 = 9$, $\theta = 60°$. (b) Similar comparison for 1:2 expansions at $\alpha = 15°$ and $25°$. $H_u = 5$, $H_0 = 4$, $\theta = 60°$.

studied by a few groups [25, 73]. In this subsection, we will examine how the speed of wicking through contractions and expansions is affected by the flow geometry. Consider a tube of total length H_t. The two radii R_1 and R_2 are prescribed, as is the upstream length H_u. The rest of the length consists of a contraction or expansion and possibly a straight downstream segment. The question is what contraction or expansion angle gives the fastest wicking through the total length. We have tested a range of contraction/expansion angles and wetting angles. A clear trend emerges, and is illustrated in Fig. 4.9 by comparing $\alpha = 15°$ and $25°$ for $\theta = 60°$.

In Fig. 4.9(a), the two trajectories coincide prior to reaching the start of the contraction, point a. Afterwards the wicking accelerates faster through the sharper contraction at $\alpha = 25°$, evidently because of the faster increase in curvature and capillary pressure. But the sharper contraction is shorter, and the acceleration ends at point b, after which the meniscus enters the narrow downstream segment and decelerates. In comparison, the milder contraction sees a more gradual acceleration that lasts longer, till point c. Downstream of point c, wicking decelerates as well, but at a gentler rate than in the sharper contraction. This is because the sharper contraction incurs more viscous friction. As a result, the meniscus eventually overtakes that in the sharper contraction, at $H_w \approx 14.8$. Therefore, the question of which geometry gives faster wicking depends on the length of the downstream segment. If it is long enough, a gentler contraction wins. If H_t and H_u are prescribed, then there is an optimal α that gives the shortest penetration time through the entire length. For example, for $H_t = 13$, $H_u = 10$, and $\theta = 60°$, we have tested α values from 15° to 65°, and $\alpha = 25°$ gives the shortest transit time.

For expansion, the story is simpler (Fig. 4.9*b*). Wicking is slower in the sharper expansion because the driving force, the capillary pressure, decreases more steeply with the expanding tube radius. This effect is so strong that the sharper expansion (from a to b) takes longer time to traverse than its milder counterpart (from a to c) despite its shorter length. Note the sudden surge of H_w at b and c when the contact line rapidly traverses the concave corner. Upon entering the downstream segment, wicking accelerates to more or less the same speed in both geometries. This speed will gradually decline in the downstream tube. Overall, the sharper expansion always causes a longer penetration time. Besides, comparing Fig. 4.9(a) and (b), the expansion takes much longer time than the contraction of the same length and same α, by 15-fold for $\alpha = 15°$, and 53-fold for 25°. This implies that in a contraction-expansion combination, the latter takes up most of the penetration time.

The penetration or passage time t_p, as it turns out, sheds unique light on the validity of the quasi-static assumption widely used in the literature. By using the formula of Liou *et al.* [47], based on a quasi-static spherical interface, we have calculated t_p through expansions at different angles. The formula overpredicts t_p by 2.5% for $\alpha = 5°$, and by 0.81% for $\alpha = 25°$. With increasing α, wicking becomes slower, giving the interface more time to relax toward equilibrium. A different picture emerges for contractions. As α increases from 5° to 25°, the underestimation of t_p by the quasi-static method increases from 16% to 32%. Evidently, a faster moving interface deviates more from the spherical shape, and renders the quasi-static assumption less accurate. At large contraction angles, however, another factor comes into play. The strong radial flow tends to restore the meniscus toward spherical (cf. Fig. 4.4*b*).

To better reflect the flow geometry in porous media, Erickson *et al.* [25] studied wicking through multiple contraction-expansion cycles. They came to the surprising conclusion that as long as the total lengths of the wide segments and narrow segments are each kept constant, the penetration time t_p remains the same regardless of the number of contraction-expansion cycles. This implies that adding additional contraction and expansion pairs costs no delay in the wicking, something inconsistent with our observations in Fig. 4.9. To probe this further, we compare wicking through three channels with $N = 1$, 2 and 3 contraction-expansion cycles (Fig. 4.10). The total

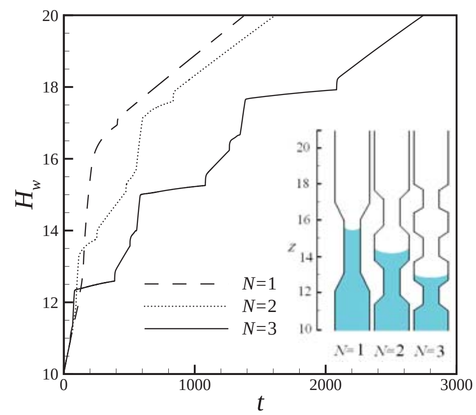

Figure 4.10: Wicking through multiple contraction-expansion cycles. For $N = 1$, 2 and 3, $\alpha = 26.6°$, $45°$ and $56.3°$. The wetting angle $\theta = 30°$, $Cn = 0.02$. The total length $H_t = 21$, and the meniscus starts at $H_0 = 10$ at the beginning.

lengths of the straight segments are the same among the three, 16 for the wider part and 3 for the narrower part. The sloping segments also add to the same length of 2, and the contraction/expansion angle then increases with N. This geometric setup is modeled after Erickson *et al.* [25]

According to Fig. 4.10, the total penetration time t_p is not the same among the three; it increases by 17% from $N = 1$ to 2 and by another 70% to $N = 3$. As expected, additional contraction-expansion pairs do cost penetration time, more so for larger N as α increases. The discrepancy is mainly because Erickson *et al.* [25] used a much smaller α ($\sim 0.5°$) and straight sections much longer than the contractions and expansions. Thus traversing the contraction and expansion takes up only a small fraction of the total t_p. Moreover, they ignored the local fluid dynamics at the meniscus and replaced it by a quasi-static spherical surface. To probe smaller α in our model, we have computed gentler slopes with α increasing from 1° at $N = 1$ to 15.6° at $N = 16$, with $\theta = 30°$, $R_2/R_1 = 0.75$, $H_u = 10$ and $H_t = 41$. Compared with $N = 1$, t_p increases by a mere 2.1% for $N = 8$ and 11% for $N = 16$. Since Erickson *et al.* [25] only investigated N up to 3, they would not have noticed much change in t_p even if they had not used the quasi-static assumption.

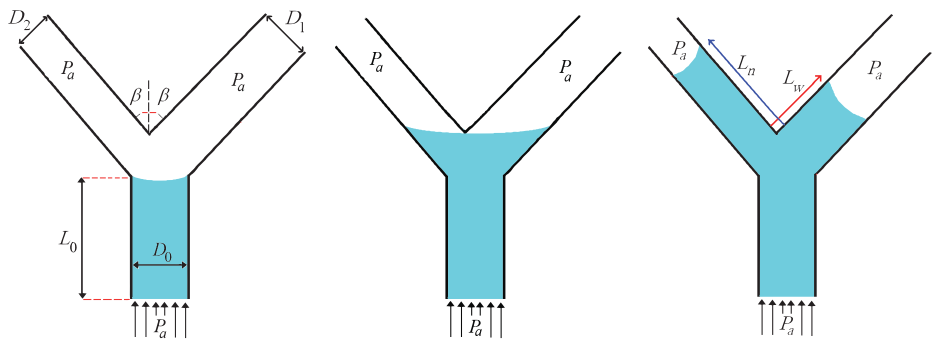

Figure 4.11: Schematic of a planar microchannel with a Y-shaped bifurcation, showing three stages of wicking: (a) the meniscus reaches the expansion; (b) the meniscus breaks into two at the bifurcation; (c) wicking continues in each branch under suitable conditions.

4.4 Wicking in Y-shaped branches: capillary competition

Connectivity between pores is an important attribute of porous media that has not been considered in the above. When the meniscus reaches the bifurcation where one pore branches into two, will it split into two and go through both branches, or will one branch dominate the other? What parameters determine the interfacial dynamics at and after the bifurcation? These are the questions that we turn to in this section.

Consider the wicking flow in the 2D planar geometry of Fig. 4.11. The same ambient pressure p_a exists at the far-upstream of the root channel and the far downstream of both branches. When the interface reaches the branching point, it breaks up into two smaller menisci (Fig. 4.11b), each then quickly adjusting to the size of the branches. A bifurcation into two identical branches is a trivial case; wicking proceeds in each branch with equal velocity. If the two branches differ in size, then there is a potential for *capillary competition* governed by the following three factors. (i) The pressure behind each meniscus depends on its curvature and hence the size of the branch. Although the interface is generally non-spherical, we can roughly speak of the capillary pressure in the wide branch p_w being higher than that in the narrow one p_n: $p_w > p_n$. The narrow channel engenders a lower capillary pressure and is thus more conducive to wicking flow. (ii) At the junction, we can roughly think of a pressure p_j that is shared by both branches. The pressure drops $p_j - p_w$ and $p_j - p_n$ drive the flow in each branch (Fig. 4.11c). (iii) p_j is determined by the viscous friction in the root tube, and continuously rises in time. This is because as wicking proceeds, the flow in one or both branches slows down and so does the flow in the root tube.

Depending on whether p_j is greater than p_w and p_n, we can differentiate two situations: wicking in both branches and wicking in one branch only. The former happens if p_w and p_n differ little, or if the pressure drop expended in the root tube is small such that p_j is initially high. The latter happens if the two branches are disparate in size, or if there is a long and thin root tube to yield a weak p_j. In discussing these two regimes in the following two subsections, we have found it convenient to fix $D_2 = 0.5D_1$ and $L_0 = 4D_1$, and vary the width of the root tube D_0 relative to D_1. In addition, the contact angle is set at $\theta = 60°$. Length will be scaled by D_1 and time by $\mu_1 D_1/\sigma$.

4.4.1 Flow in both branches

With a wide root tube, the viscous dissipation in it is small and it is like connecting the branches directly to a reservoir. In this simple situation, wicking occurs through both branches, though at different speeds depending on their size (Fig. 4.12).

When the meniscus reaches the end of the root tube (Fig. 4.11a), it faces an expansion at angle β, and the discussion of pinning in §4.3.3 applies. In particular, we require $\beta < 90° - \theta$ such that the meniscus can depin from the corner and proceed beyond this point. Throughout this section we have used $\beta = 20°$. When the interface reaches the point of bifurcation (Fig. 4.11b), it breaks into two smaller menisci, whose curvature, at this point, reflects the larger dimension of the junction. Thus they are not at equilibrium with the smaller size of each branch. A short period of equilibration ensues, with the wall points on the outside walls pulling back and those on the walls in the middle surging ahead. This is why in Fig. 4.12 the curves appear to start from a small positive L value at $t = 0$. In the inset, points a and b mark when the equilibration is completed in the narrow and wide branches, respectively. Note that the bifurcation angle β determines the size of the meniscus in Fig. 4.11(b) and the equilibration process. But it has little effect on the subsequent wicking in each branch. Once the equilibration is completed, each meniscus is orientated symmetrically with respect to the axis of its branch. The geometric setup is such that the pressure p_j is higher

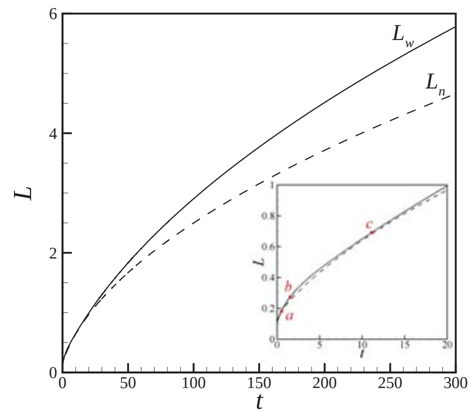

Figure 4.12: Wicking in both branches with a relatively wide root tube: $D_0 = 1.6$. The origin of time is when the meniscus first touches the tip at the junction (cf. Fig. 4.11b). The inset shows that wicking is faster in the narrow branch initially ($t < 11$) but the wide branch winns for longer times.

than both p_n and p_w, and wicking proceeds in both branches.

Initially, the narrow tube enjoys faster wicking because the pressure drop $p_j - p_n$ driving the flow is larger than its counterpart in the wide tube. This lasts till $t \approx 11$, marked by point c in the inset of Fig. 4.12. As the liquid continues to invade both branches, the viscous dissipation increases with the column height and the flow speed declines. This effect is stronger for the narrow branch since, as the flow approaches the Poiseuille flow, the viscous wall stress scales with the meniscus velocity divided by the channel width. Thus, the wider tube has faster wicking for later times, similar to the prediction of the Lucas-Washburn equation.

Once the flow starts in either branch, it does not stop in finite time. This is because p_j must exceed the pressure p_n or p_w for there to be flow in the branch. In time p_j and hence the pressure drop only increase as the flow and pressure drop in the root tube declines. Thus, the flow continues in both branches, and gradually slows down toward zero in time.

4.4.2 Flow in one branch

With thinner root tubes, p_j may initially fall below the capillary pressure p_w in the wide branch such that wicking occurs only in the narrow branch.

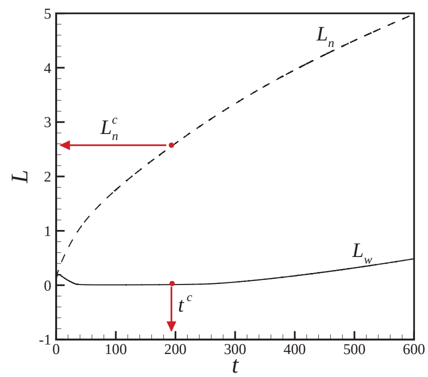

Figure 4.13: Capillary competition between two branches with a relatively narrow root tube, $D_0 = 0.6$. Wicking proceeds in the narrow branch but is suppressed in the wide branch until $t^c = 194$, marked by a dot on both curves. The origin of time is when the meniscus first touches the tip at the junction (cf. Fig. 4.11b).

This behavior is demonstrated for $D_0 = 0.6$ by the trajectories of the menisci in Fig. 4.13 and by the snapshots of the interface in Fig. 4.14. After the interface splits into two at the bifurcation, they reorient with respect to the axes of the branches and adjust their curvature to the local tube size (Fig. 4.14b). Afterwards wicking starts in the narrow branch, and the flow in the root tube entails a pressure drop. The junction pressure p_j thus produced turns out to be lower than the capillary pressure p_w in the wide branch, and no wicking occurs there. In fact, the negative pressure $p_j - p_w$ causes the interface to *retreat* until the contact line becomes pinned at the inner corner at $t = 42$. Fig. 4.14(c) depicts a moment soon afterwards with the meniscus immobilized in the wide branch. But the arrest of flow in the wide branch is necessarily temporary. As the flow slows down in the narrow tube, p_j rises continually, eventually surpassing p_w to produce wicking flow in the wide branch as well. This is marked in Fig. 4.13 by $t^c = 194$ when the liquid column in the narrow tube is at $L_n^c = 2.56$. After that the situation becomes qualitatively the same as in Fig. 4.12, and Fig. 4.14(d) shows a snapshot in this stage. Eventually wicking slows down toward zero in both branches.

The onset of wicking in the wide branch, indicated by t^c or L_n^c, is of practical interest. For instance, in a porous medium of finite thickness, the critical value L_n^c for the small pores will determine whether the bigger pores

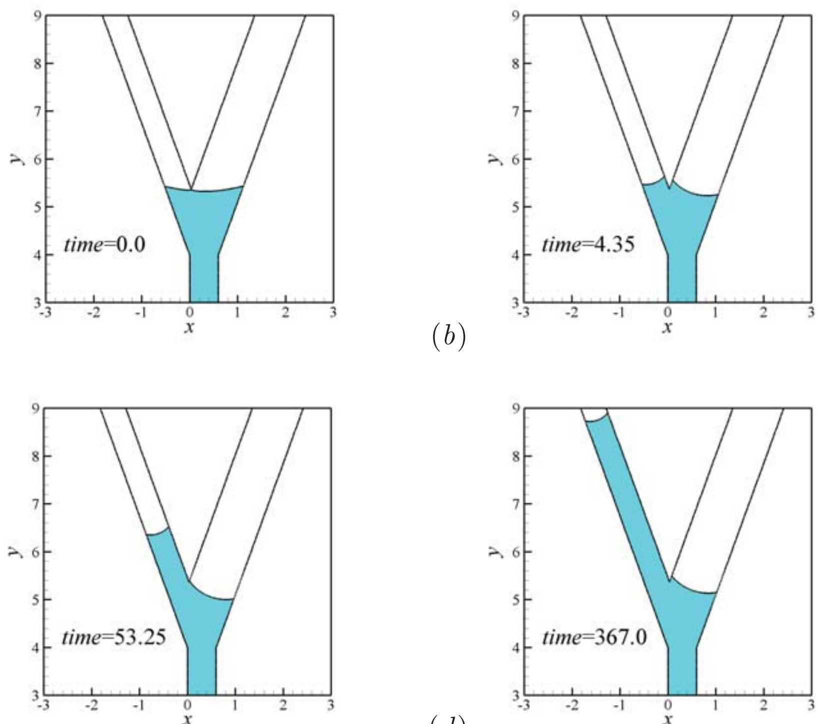

(a) (b) (c) (d)

Figure 4.14: Evolution of the interfacial morphology for the simulation depicted in Fig. 4.13. (*a*) The meniscus touches the salient corner at $t = 0$. (*b*) The meniscus relaxes toward the equilibrium curvature inside each branch. (*c*) After a brief retraction, the meniscus is immobilized in the wide branch. (*d*) After the restarting of flow in the wide branch, the menisci advance in both branches.

will contribute to liquid transport at all. If the liquid traverses the entire length of the smaller pores before wicking even starts in the bigger ones, the latter will be dead ends, which have been observed in experiments [33] and considered a major hinderance to water transport through the GDM of fuel cells [48]. Note that all the ideas and qualitative arguments discussed so far in this section apply as well to 3D flows in real porous media.

In the spirit of the Lucas-Washburn analysis (Eq. 4.2), we can estimate the onset of wicking in the wide branch by neglecting dynamics at the menisci and assuming fully developed Poiseuille flow in the root and narrow tubes. Let us denote the instantaneous average velocity in the narrow tube by V_2 and that in the root tube by V_0. Then the junction pressure p_j can be estimated either from the force balance on the liquid in the root tube or that in the narrow tube:

$$p_j = p_a - \frac{12\mu L_0 V_0}{D_0^2} = p_a - \frac{2\sigma\cos\theta}{D_2} - \frac{12\mu L_n V_2}{D_2^2}. \tag{4.4}$$

The critical condition for wicking in the wide tube is p_j being equal to the capillary pressure behind the meniscus in the wide tube:

$$p_j = p_w = p_a - \frac{2\sigma\cos\theta}{D_1}. \tag{4.5}$$

In addition, volume conservation requires $V_0 D_0 = V_2 D_2$. Eliminating V_0 and V_2 from the above gives the following critical condition on the liquid column L_n^c:

$$L_n^c = L_0 \left(\frac{D_1}{D_2} - 1\right)\left(\frac{D_2}{D_0}\right)^3. \tag{4.6}$$

Recall our previous argument that wicking in the wide tube depends on the viscous friction in the root tube and the dissimilarity between the two branches. It is no surprise that L_n^c turns out to depend on the length and diameter of the root tube as well as the size difference between the two branches. For the conditions in Fig. 4.13, Eq. (4.6) predicts $L_n^c = 2.3$, reasonably close to the numerical result of 2.56. Numerical experimentation with narrower D_0 values has confirmed further delays in the wide branch in agreement with Eq. (4.6). Finally, we note that the above calculation can be easily generalized to 3D circular tubes, and the formula has the exponent on (D_2/D_0) changed from 3 to 4.

4.4.3 Flow reversal due to spatially inhomogeneous hydrophilicity

Insofar as the Young-Laplace equation gives a capillary pressure in the form of $\sigma\cos\theta/D$, varying the contact angle θ in a branch is in a way tantamount to varying the tube size D. Thus, capillary competition between branches can be controlled by varying θ as well as D. Suppose that in Fig. 4.11, we make the downstream portion of the wide branch more hydrophilic, with a smaller contact angle. Then a *flow reversal* may occur in the narrow channel, as illustrated in Fig. 4.15.

In this geometry, $\theta = 60°$ throughout the Y-branch except for the downstream portion of the wide branch starting from $L_w = 1.25$ that features

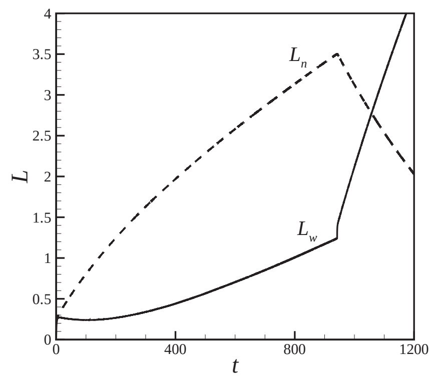

Figure 4.15: Flow reversal in the narrow branch when the meniscus in the wide branch moves onto a more hydrophilic portion with $\theta = 20°$ at $L_w = 1.25$. Elsewhere $\theta = 60°$. $D_0 = 0.6$, $L_0 = 4$, $D_2 = 0.9$.

a smaller $\theta = 20°$. The geometric and physical parameters of the setup are such that wicking occurs initially only in the narrow branch, and starts later in the wide channel around $t = 110$. When the meniscus encounters the more hydrophilic portion in the wide branch ($t = 942$), the wicking suddenly accelerates, causing a flow reversal in the narrow tube. This is because the elevated flow rate in the root tube depresses the pressure at the junction so much that it falls below the capillary suction pressure p_n in the narrow tube.

Depending on the physical and geometric parameters, the liquid column may retreat entirely from the narrow tube, with the interface pinned at the corner of the bifurcation, or reverse its course again before that. Thereafter, the situation becomes similar to Fig. 4.13 or Fig. 4.12. Based on the Young-Laplace equation, one may view the wicking in the more hydrophilic portion of the wide branch as occurring in a tube with $\theta = 60°$ but a *smaller effective width* $D_e = D_1 \cos 60°/\cos 20° = 0.53D_1$, which is narrower than D_2. (The viscous friction will be different, of course.) Thus, the wicking continues with dwindling speed in the wide branch until the junction pressure has again risen above the capillary pressure in the narrow tube to restart wicking there.

Such flow reversal has been observed experimentally. Litster *et al.* [48] reported that in a model GDM for fuel cells, a sudden acceleration in one flow path, due to breakthrough from the GDM into open space, causes the liquid to retreat in a neighboring connected path. The underlying principle is simple and robust, and suggests how surface properties can be manipulated to control the flow pattern in porous media. Indeed, the GDM of fuel cells is often surface-treated in a spatially inhomogeneous way to enhance water transport [46]. In addition, a more hydrophilic micro-porous layer with finer pores is often attached to the GDM to create a jump in wettability along the flow direction [78]. Another potential application for capillary competition and flow reversal is as a precise switching mechanism in microfluidic devices [7, 16, 44]. By careful choice of the root and branch sizes it is possible to design a flow loop in which different branches are impregnated by liquid at precise moments. The mechanism of capillary competition works for multiple branches as well, and one may design microfluidic manifolds using the same principle.

4.5 Summary and conclusions

This work aims for a detailed and rational understanding of two-phase transport through micropores in porous media. Using finite-element computations, we capture the evolving morphology of the interfaces in geometries that retain the salient features of real pores, including expansion, contraction and branching. From a fundamental viewpoint, the most important findings are the following:

(a) The meniscus undergoes complex deformation during transit through micropores, governed by the dynamic balance among fluid-solid and gas-liquid interfacial tensions and viscous friction. Such flow effects tend to distort the meniscus away from a spherical shape.

(b) The dynamics of the contact line plays a central role. It pins at protruding corners, potentially barring wicking into expansions with too steep a slope. The contact line negotiates inner corners thanks to the diffuseness of the interface.

(c) Capillary competition between connected branches depends on the capillary pressure due to meniscus curvature inside each, and in turn on the size of the branches and surface wettability. Under suitable conditions, wicking can be arrested in wider branches in favor of a narrower one, and the flow may even reverse course when wicking accelerates in a neighboring path.

We have hinted at the relevance of these insights to technological applications, e.g., in proton-membrane exchange fuel cells. Against this background, however, the work reported here must be seen as a preliminary step. Real 3D flow through porous media includes many complicating factors that have not been accounted for, including 3D connectivity, pore size distribution and tortuosity of the flow path. Nevertheless, this serves as a starting point for an approach to two-phase flow in porous media that is more rational and accurate than the traditional one centered on an empirical relative permeability.

Chapter 5

Auto-ejection of Liquid Drops from Capillary Tubes

5.1 Introduction

Droplet production is a fluid dynamical process of considerable importance in engineering applications. The rapid development of microfluidic technology has given new impetus to the study of controlled drop production in miniaturized devices [31]. A common method for drop production is to pump liquid through a tube such that a jet issues from the end, and breaks up due to capillary instability. In microfluidics, this is typically realized by flow focusing [4, 77], and two regimes, jetting and dripping, have been identified [2, 84, 99]. Jet breakup can be actively promoted and controlled by a pressure pulse, as in drop-on-demand devices [91]. In these schemes of drop formation, the jet is always fed by an externally controlled flow rate.

As mentioned in Chapter 1, Wollman and coworkers have demonstrated a novel method of drop formation that relies on wicking in a capillary tube [86, 87, 88]. Two interesting questions can be asked about this process: what the critical condition is for ejecting one or more drops, and how geometric parameters of the problem affect the ejection. The ejection process is governed by inertia as well as capillarity, much like for Worthington jets [30] and cavity jets [5]. Regarding the first question, it seems reasonable to argue that auto-ejection occurs when the upward momentum of the liquid column overcomes capillary restriction of the liquid surface. As will be shown later, viscous friction is negligible under typical experimental conditions. However, it is difficult to quantify this idea in terms of a Weber number. This is because both the liquid momentum and the capillary restriction vary in time as complex functions of several factors, including the dynamic contact angle, the shape of the nozzle and contact line pinning. In particular, auto-ejection has never been recorded at the end of a straight tube; the converging nozzle seems to be necessary [70, 88].

To analyze this intricate process, it seems appropriate to divide it into two stages, the acceleration of the meniscus inside the tube, including the nozzle at the end, and the protrusion and possible breakup of the jet outside the nozzle. In the following, we will briefly summarize the current state of knowledge on each phenomenon.

Capillary rise inside straight tubes has been extensively studied before; see for example [72]. In the absence of gravity, the dynamics is mainly governed by the interplay among capillary, viscous and inertial forces. At the initial stage of the rise, viscous forces are negligible and the balance between capillary and inertial forces yields a constant rise velocity [64]:

$$v_{ci} = \left(\frac{2\sigma \cos\theta_d}{\rho R} \right)^{\frac{1}{2}}, \tag{5.1}$$

where R is the tube radius, ρ is the liquid density, σ is the surface tension and θ_d is the dynamic contact angle. This is known as the capillary-inertial velocity. As the imbibition proceeds, the liquid column increases in length and mass. Viscous friction becomes important and the meniscus velocity starts to decline. Eventually inertia becomes unimportant and the dynamics enters the Lucas-Washburn regime where capillary pressure balances the viscous friction [49, 85]. Denoting the liquid viscosity by μ, we can write the velocity of rise as

$$v_{LW} = \frac{R\sigma \cos\theta_d}{4\mu H}, \tag{5.2}$$

which decreases with the length of the liquid column H. The above are two limiting behaviors for short and long times. In the auto-ejection process, however, it is not clear *a priori* if the meniscus velocity follows either equation. What is more, these simple models disregard the contact line dynamics. At high velocities, the dynamic contact angle θ_d may deviate considerably from the static one θ [11, 38]. Thus, the capillary force driving the meniscus changes with its velocity, adding another subtlety to the problem.

As the nozzle is essential for auto-ejection, the meniscus acceleration inside the nozzle is a key aspect of the process. For inertialess flows, [51] have investigated the meniscus dynamics inside contractions, including the transient turning of the interface, its evolving curvature as well as the overall acceleration of the liquid column. Auto-ejection requires a high incoming momentum with a large inertia, and the meniscus dynamics inside the nozzle remains to be studied.

In the second stage of auto-ejection, a jet emanates from the nozzle, and one or more droplets form through a capillary mechanism known as end-pinching [74]. Essentially, capillary retraction at the tip produces a bulbous end, whose neck then becomes susceptible to capillary pinch-off. End-pinching has been studied by linear instability analysis [45], one-dimensional lubrication model [3], experiments [15, 83] and numerical simulations [36, 56, 67, 82]. These studies have assumed either zero incoming flow at the base of the jet or a constant flow rate. Work of Gordillo and Gekle [34] appears to be the only one that allows a transient incoming flow; a linearly decreasing incoming velocity is assumed for Worthington jets. The auto-ejection problem differs in that the jet is being fed by a time-dependent flow rate that is governed by the morphology of the jet and the physical conditions inside the tube and nozzle. Thus, spatial and temporal variations of the liquid velocity determine the fate of the jet and the number and size of any droplets that may form. Prior studies have indicated additional geometric complications related to the shape and wettability of the lip of the nozzle [2]. How the interface may depin from the inner edge of the lip and move along its width turns out to have a strong influence on drop pinch-off.

The review of prior work suggests the criterion for auto-ejection to be the most prominent question. To answer this question, one must study the meniscus dynamics in the tube and the nozzle, as well as the jet behavior outside. In particular, the criterion should predict how auto-ejection depends on geometric factors: tube length, contraction angle, and even the width of the lip at the exit of the nozzle. We undertake such an investigation using numerical simulations that captures detailed features of the contact line dynamics.

5.2 Problem setup

The axisymmetric computational domain consists of a capillary tube connected to a liquid reservoir at the bottom and ambient air at the top (Fig. 5.1). In most of the simulations the tube has a contracting nozzle at its upper end. The contraction angle is α and the radius shrinks from the tube radius R to R_n at the end of the nozzle. The total length of the tube, including the nozzle, is L. Thus, the flow geometry is completely specified by three dimensionless quantities: the contraction angle α, the contraction ratio $C = R_n/R$ and the aspect ratio L/R. Initially the air-liquid interface is assumed flat at a small distance L_0 inside the tube. For the most part, L_0 represents the capillary climb under normal gravity before the drop-tower experiment commences [88]. There is also a numerical incentive for placing the interface inside the tube to avoid complications at the corner.

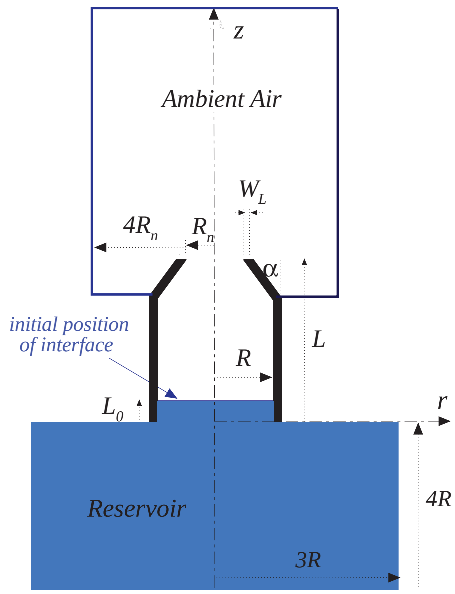

Figure 5.1: Schematic of meridian plane of the axisymmetric computational domain.

The liquid and air reservoirs are sufficiently large that their boundaries have no effect on dynamics of the meniscus, liquid jet and drops. Based on numerical experiments, we have chosen the liquid reservoir to be $3R$ in radius and $4R$ in height. On its bottom and side walls, we impose zero normal stress and zero tangential velocity as boundary conditions. Its top wall is taken to have zero shear stress and zero normal velocity. This boundary condition avoids the computational cost of tracking the slight deformation of the liquid-air interface outside the tube. [72] have shown that this simplification has little effect on the meniscus motion, and we have reached the same conclusion by benchmarking our simulation of capillary rise against experiments. The air reservoir on top is $4R_n$ in radius, and its height ranges from $12R_n$ to $30R_n$ depending on the length of the ligament in different simulations. Zero stress boundary conditions are used on the top, bottom and side of the air reservoir. On the sloping walls of the nozzle, no-slip conditions are imposed. The upper surface of the nozzle (or the "lip") is a horizontal ring of width W_l. For most of the simulations, this surface is assigned a contact angle $\theta_l = 180°$ to ensure that the contact line remains pinned at the inner corner of the lip. Smaller θ_l values are used in §5.4.4 to explore depinning of the interface from the sharp corner.

In addition to the geometric ratios, the problem is characterized by four dimensionless groups based on material properties: the liquid-air density ratio ρ/ρ_a and viscosity ratio μ/μ_a, the Ohnesorge number $Oh = \mu/\sqrt{\rho R \sigma}$, and the static contact angle θ inside the tube and nozzle. On the inner surface of the tube, we impose the no-slip condition, and model the motion of the three-phase contact line by Cahn-Hilliard diffusion to be discussed below. Gravity is neglected in all presented results except in Fig. 5.10. This is because most of the experimental data have been collected under microgravity, and gravity tends to inhibit auto-ejection. We will fix these parameters: $\theta = 0°$ (perfect wetting), $\rho/\rho_a = 200$ and $\mu/\mu_a = 100$. In comparison with the silicone oils used in the experiments [88], the density ratio is too low but the viscosity ratio is within the range of experimental values. In view of the numerical difficulties in computing larger density ratios, we are satisfied that the air has little influence on the liquid jet and drops [28]. We will vary the three geometric ratios C, α and L/R along with the Ohnesorge number Oh. We will use R as the characteristic length, the capillary-inertial time $t_{ci} = \sqrt{\rho R^3/\sigma}$ as the characteristic time, and R/t_{ci} as the characteristic velocity, and present the results in dimensionless form.

5.3 Physical model and numerical algorithm

From a computational viewpoint, the auto-ejection process is difficult to simulate as the interface moves, deforms and eventually breaks up, and the process features a prominent role for the moving contact line.

As discussed in Chapter 2, our diffuse-interface model leaves us with three new model parameters, say ϵ, γ and Γ. We follow the procedure recommended by [93, 94] to choose their values. For smallest value of ϵ which is computationally affordable, γ is chosen to ensure that the sharp-interface limit is achieved. Then value for the wall relaxation parameter Γ is determined by fitting an experimental datum.

To implement this procedure, we make the parameters dimensionless using a characteristic length l_c: $Cn = \epsilon/l_c$, $S = l_d/l_c$, and $\Pi = 1/(\Gamma \mu l_c)$. Cn is commonly known as the Cahn number [100]. One needs to be careful in choosing l_c. Accurate simulation using the diffuse-interface model requires that the interfacial thickness ϵ and the diffusion length l_d both be much smaller than the global length scale [93]. As the meniscus advances through the nozzle, the effective global length scale is shrinking. We find it necessary to reduce ϵ and l_d accordingly to maintain accuracy of the simulation.

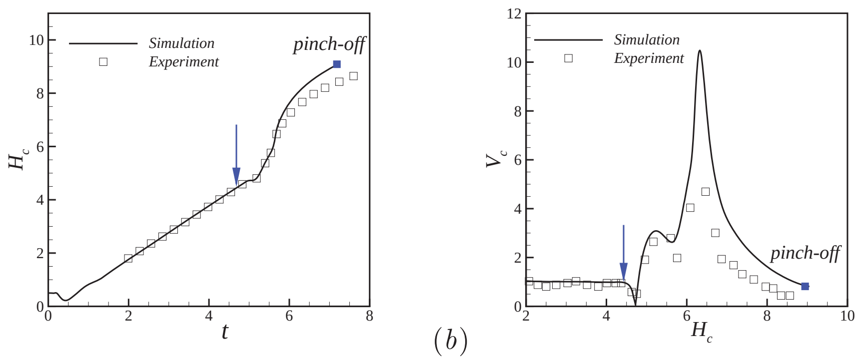

Figure 5.2: With a wall relaxation parameter $\Pi = 0.4$, the simulation approximates experimental results closely in terms of (a) the position of the center of the meniscus, and (b) the centerline velocity of the meniscus. The arrows indicate the moment when the contact line reaches the start of the nozzle, and the curves end when a drop pinches off, indicated by a filled square. The geometric and physical parameters match the experiment of [86]: $Oh = 0.011$, $L = 5.98$, $C = 0.493$, $\alpha = 23.8°$ and $\theta = 0°$. In addition, $S = 8 \times 10^{-3}$ and $C_n = 0.01$.

Therefore, when the contact line is in the straight portion of the tube, we take $l_c = R$. When it is in the nozzle, we take l_c to be the local radius of the nozzle at the contact line. After the contact line reaches the lip, we fix $l_c = R_n$. Thus, with fixed values of Cn, S and Π, the microscopic lengths ϵ and l_d shrink inside the nozzle as required.

We determine the model parameters by the experiment of [87] on capillary ejection. The geometric and material parameters are matched such that $Oh = 0.011$, $L = 5.98$, $C = 0.493$, $\alpha = 23.8°$. The static contact angle is 0° inside the tube and 40° degrees outside. The initial height of the liquid column $L_0 = 0.08L$ matches the experiment condition at the start. Following [94], we choose a small Cahn number $Cn = 10^{-2}$ that is comfortably computable, and a corresponding $S = 8\times10^{-3}$. Then we found that $\Pi = 0.4$ gives the closest agreement with the experimental results. This is illustrated in Fig. 5.2 in terms of the position and velocity of the center of the meniscus. A notable feature of this simulation is the evolution of the dynamic contact angle θ_d. The wall energy relaxation in equation (2.12) allows θ_d to deviate from θ [94]. Fig. 5.3 compares our computed θ_d for capillary rise in a straight tube with two experimental correlations. In our computation, the meniscus rises with an essentially constant speed V, with which we define a capillary number $Ca = \mu V/\sigma$. The correlation of Ref. [11] is for solid strips drawn

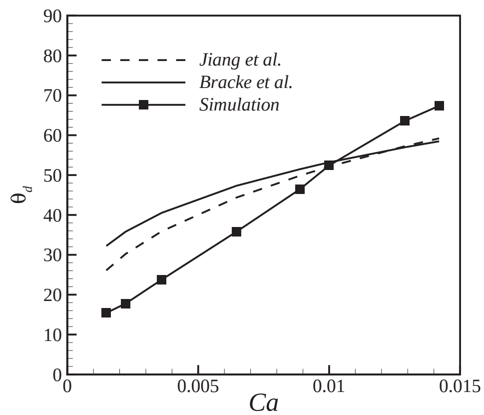

Figure 5.3: Comparison of the dynamic contact angle θ_d in a straight tube between our numerical simulation and two experimental correlations due to [41] and [11]. The model parameters are the same as in Fig. 5.2.

into a pool of liquid, while that of Ref. [41] is based on the experiments of Hoffman [38] on pushing non-polar liquids through glass capillary tubes. The numerical and experimental results all indicate an increase of θ_d with Ca, but the former exhibits a somewhat steeper slope than the experiments. One reason for the difference is that the Cahn-Hilliard model is phenomenological, and the mechanism of wall energy relaxation cannot be expected to capture quantitatively the dynamic contact angle. Moreover, in our simulations θ_d is measured from the slope of the interface where it intersects the wall. In the experiments, it is estimated from fitting a circular arc to the central portion of the meniscus. This introduces some discrepancy as well.

5.4 Results

5.4.1 Meniscus dynamics

We begin with an overview of the dynamics of the meniscus as it advances through the straight portion of the tube and the contracting nozzle, and forms a jet outside the nozzle. For this purpose we select a typical set of physical and geometric parameters: $Oh = 0.01$, $L = 5$, $C = 0.5$, $\alpha = 30°$ and $\theta = 0°$. To describe the motion and deformation of the meniscus, we track the contact line velocity along the wall V_w and the velocity at the center of the meniscus V_c in time.

Fig. 5.4(a) plots V_w and V_c, as well as the average velocity across the nozzle exit V_n, as functions of time. Before the liquid meniscus arrives at the nozzle exit, V_n is computed from the velocity profile of air. From an initially flat shape (Fig. 5.1), the meniscus experiences an acceleration and adjustment phase at the start of the imbibition. The contact line immediately moves upward at a roughly constant speed, while the center of the meniscus oscillates several times before settling into a steady shape and speed of rise (point a in Fig. 5.4). This marks the start of the capillary-inertial regime. The meniscus velocity $V_w = V_c = 1.09$ agrees closely with the theoretical result $v_{ci} = 1.07$ (cf. equation (5.1)). This steady rise persists till point b, when the contact line arrives at the start of the nozzle. It is remarkable that the meniscus velocity stays roughly constant so far, showing little decrease due to viscous dissipation. This can be rationalized by an estimation of the viscous effect in a straight tube. By balancing the capillary, viscous and inertial forces, Bosanquet [8] derived an analytical solution for the rise of the meniscus. For short times ($Oh \cdot t \ll 1$), this solution predicts the following variation of the meniscus velocity along the tube:

$$\frac{1}{V_c}\frac{dV_c}{dH_c} = 2.4\ Oh, \tag{5.3}$$

where V_c and H_c are dimensionless. Our numerical simulation verifies the proportionality to Oh, but with a milder slope of 1.8. For $Oh = 0.01$ and an axial distance of about 2.5 for the capillary-inertial regime in Fig. 5.4, therefore, viscous reduction of the meniscus velocity V_c is only about 5%. In fact, viscosity never plays an appreciable role throughout the entire process, and will be disregarded for the rest of the chapter. In the experiments, Oh is typically on the order of 0.01 [88], and viscosity is generally immaterial.

Once the contact line reaches the nozzle, the interface immediately rotates at the contact line so as to adjust its orientation relative to the tapering wall of the nozzle. This rotation pushes the central portion of the meniscus backward by capillarity, thus reducing the centerline velocity V_c to a minimum at point c in Fig. 5.4. Afterwards, the meniscus accelerates rapidly upward, mainly because of the upward momentum of the liquid column being channeled through a narrowing conduit. Capillarity also contributes to the acceleration since the meniscus is trailing the spherical shape at the moment, having been delayed by the rotation of the interface from b to c. This is illustrated in the snapshots of the interfaces in Fig. 5.4. This stage continues until point d, when the upward acceleration has moved the central portion of the meniscus ahead of the spherical surface dictated by the

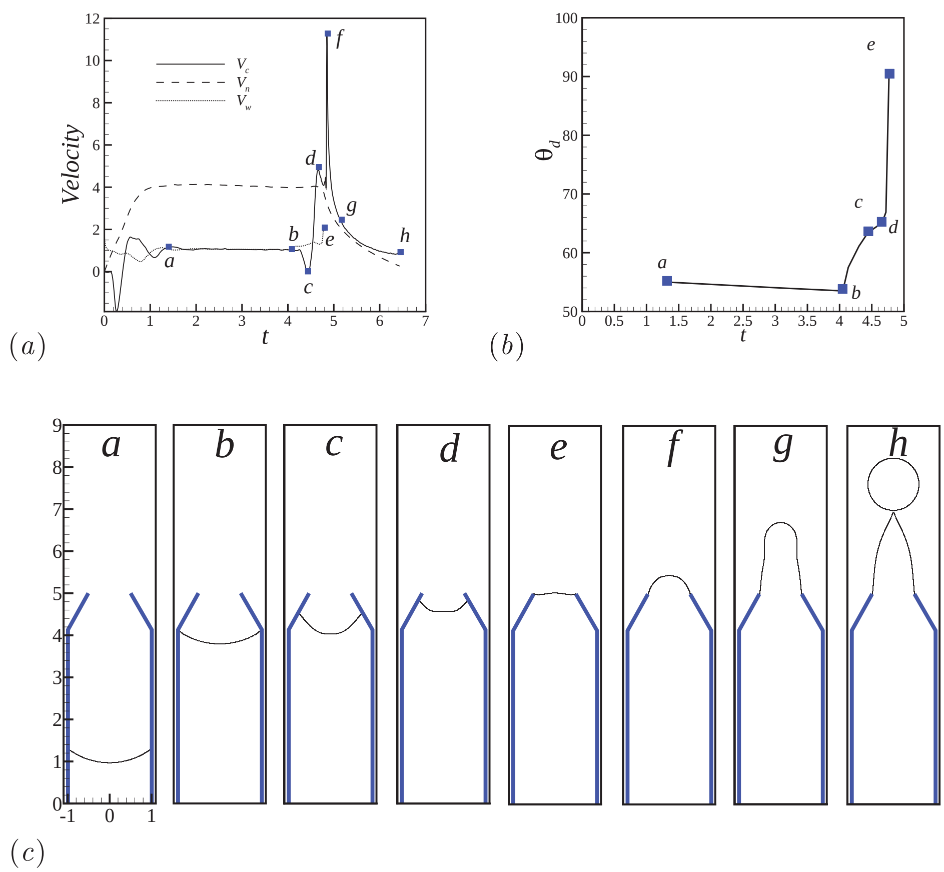

Figure 5.4: (a) Evolution of the contact line velocity V_w, meniscus center velocity V_c, and average velocity at nozzle exit V_n in time. (b) Evolution of the dynamic contact angle θ_d. (c) Snapshots showing the position and shape of the meniscus at significant moments marked in the velocity plot. $Oh = 0.01$, $\theta = 0°$, $L = 5$, $C = 0.5$ and $\alpha = 30°$.

local dynamic contact angle. Thus capillary forces now pull the meniscus backward, causing the reduction in V_c until point e, when the contact line reaches the lip of the exit. Note that with the contact line inside the nozzle, the contact line speed V_w is still measured by the axial position of the contact line, not by the distance traveled along the wall. Fig. 5.4(b) shows that from point a till point e, the dynamic contact angle θ_d closely tracks the evolution of the contact line speed V_w, in accordance with the observations in Fig. 5.3.

At point e, the contact line becomes pinned at the sharp inner corner of the lip according to Gibb's criterion [27, e.g.]. Constraining the upward flow near the nozzle wall results in a high pressure at the nozzle exit that thrusts the central portion of the meniscus out in the form of a jet (point f). As the jet is ejected and lengthens against surface tension, its tip velocity declines toward point g, when capillary necking commences on the jet, eventually leading to a droplet pinching off at the tip (point h).

It is interesting to contrast the behavior of the average velocity at the nozzle, V_n, with that of the meniscus velocity V_c. Note that because of incompressibility, V_n gives the average liquid velocity in the tube (subject to a factor C^2 due to area contraction) even before the meniscus reaches the lip of the nozzle. During the initial acceleration of the meniscus, prior to point a, V_n monotonically increases to a constant level that corresponds to the capillary-inertial regime. It starts to decline near point d, when capillarity starts to oppose the upward motion of the liquid. The decline continues monotonically even as the jet rapidly issues from the nozzle. This can be rationalized from how the interfacial tension, acting on the pinned contact line, continually depletes the upward momentum of the liquid column.

The decline of $V_n(t)$ in time after the jet formation (roughly from point f onward) can be quantified from an energy argument. Consider a control volume that encloses the inside of the tube and the nozzle, as well as the liquid reservoir. The kinetic energy of the liquid inside, E, decreases because of the energy eflux at the nozzle as well as the pressure work there:

$$\frac{dE}{dt} = -\frac{1}{2}\pi R_n^2 \rho V_n^3 - p_n \pi R_n^2 V_n, \tag{5.4}$$

where p_n is the liquid pressure at the exit of the nozzle. Note that the pressure in the reservoir equal that in the ambient, and has been put to zero, and that the incoming energy flux has been neglected as the velocity at the boundary the reservoir is much smaller than that inside the capillary tube. E is the sum of the kinetic energy in the tube, the nozzle and the reservoir. To estimate the fluid velocity inside the nozzle, we make a one-dimensional plug flow approximation by assuming that the liquid velocity is axial, and changes from V_n at the nozzle exit to C^2V_n inside the capillary tube. Similarly, the flow in the reservoir is assumed to be radial and uniform on spherical surfaces centered at the entry of the tube, with a velocity that can be related to V_n through mass conservation [76]. Thus, E can be expressed in terms of V_n:

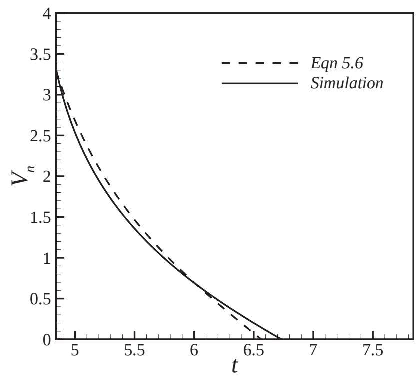

Figure 5.5: Temporal variation of the instantaneous velocity $V_n(t)$ at the nozzle exit, starting from point f at $t_f = 4.85$. $L = 5$, $Oh = 0.01, \alpha = 30°, C = 0.5, \theta = 0$, $L_e = 1.68$, $We = 7.0$.

$E \approx \frac{\pi}{2}\rho R_n^2 L_e V_n^2$, where the *effective length*

$$L_e = RC\frac{(1-C)^2}{\tan\alpha} + \left(L + \frac{7}{6}R\right)C^2 \tag{5.5}$$

is a purely geometric parameter. To estimate the exit pressure p_n, we note that the capillary pressure decreases from $2\sigma/R_n$ to σ/R_n as the liquid interface inflates from a semi-spherical shape to a cylinder with radius R_n. Taking $p_n = 2\sigma/R_n$, plugging E into equation (5.4) and integrating in time, we obtain

$$V_n(t) = u\tan\left[-\frac{u(t-t_f)}{2L_e} + \tan^{-1}\left(\frac{V_f}{u}\right)\right] = V_f\frac{1 - \frac{u}{V_f}\tan\left[\frac{u(t-t_f)}{2L_e}\right]}{1 + \frac{V_f}{u}\tan\left[\frac{u(t-t_f)}{2L_e}\right]}, \tag{5.6}$$

where $u = (\frac{2\sigma}{\rho R_n})^{1/2}$, t_f is the starting time for the integration, at point f, when the average velocity across the nozzle exit is $V_f = V_n(t_f)$.

Fig. 5.5 compares $V_n(t)$ predicted from the simple one-dimensional model and the numerical solution. At the start, the model slightly underestimates the rate of deceleration. Toward the end, however, it overestimates it as the capillary pressure at the exit falls below $2\sigma/R_n$ and approaches σ/R_n. In simulations the velocity profile is not a perfect plug flow. Such deviations from plug flow, have compensated for the overestimation of the capillary pressure.

But over the course of the deceleration of the jet, the simple model captures reasonably well the dynamics of the jet velocity. In particular, note how L_e dictates the rate of decrease of V_n in time; a larger L_e implies a longer liquid column moving with a greater kinetic energy. Thus, the deceleration will be slower, and a longer jet will likely be produced, in favor of auto-ejection. This point will be revisited in the next subsection. Finally, we have also confirmed that for the small Oh tested, viscous dissipation makes a very small contribution to the energy balance of equation (5.4), consistent with previous arguments on the unimportance of viscosity in the process.

5.4.2 Ejection criterion

Naturally, we think of a Weber number to represent the idea that the upward momentum must overcome the capillary restriction. However, there are two difficulties in constructing such a Weber number. First, there is no obvious characteristic velocity. The meniscus velocity is itself determined by the wicking inside the tube, and in turn by the contact angle and geometry (especially length) of the tube and nozzle. It also changes in time and in space. Wollman et al. [88] suggested an *instantaneous Weber number* defined using the liquid velocity at the exit of the nozzle when the meniscus first reaches that point. This corresponds to our point e in Fig. 5.4. Let us take this point as the nominal start of the jet-formation process $t^* = 0$, with $t^* = t - t_e$ measuring the time from this point onward. Using the velocity $V_e = V_n(t_e)$ at this point, we can define an instantaneous Weber number:

$$We = \frac{\rho V_e^2 R_n}{\sigma}. \tag{5.7}$$

Second, the instantaneous velocity V_e or We does not completely determine the fate of the jet and breakup. Fig. 5.6(a) shows that We does not delineate sharply the boundaries separating no-pinchoff and pinchoff, nor among different number of droplets produced. This inadequacy is not hard to appreciate. Roughly speaking, the eventual length of the jet is determined by converting the kinetic energy of the entire liquid column at $t^* = 0$ into surface energy. Thus, the length of the liquid column should matter as well. Fig. 5.6(b) shows that under conditions that are otherwise identical to Fig. 5.4, a shorter capillary tube ($L = 1.5$) produces a short jet and no breakup, whereas the longer tube ($L = 5$) of Fig. 5.4 does lead to auto-ejection. The Weber number $We = 7$ in both cases. Since we have previously introduced an effective tube length L_e (equation 5.5), it seems

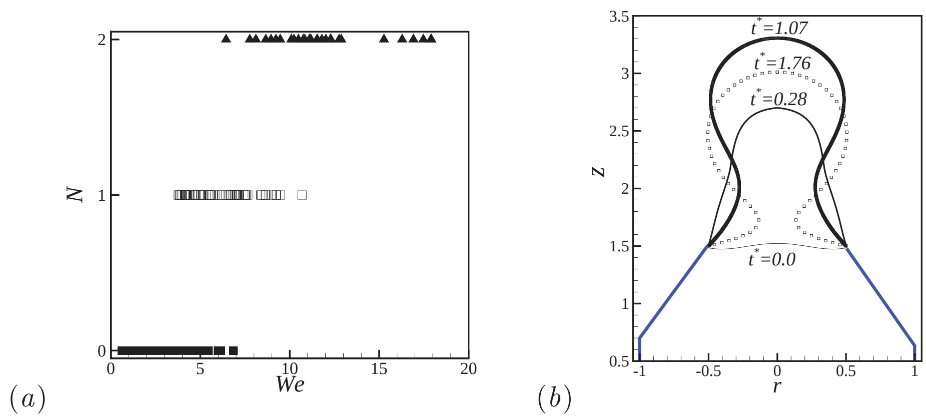

Figure 5.6: (a) Number of drops produced as a function of We. The wide overlaps between different outcomes indicate that We does not provide an adequate criterion for auto-ejection of droplets. These data cover most of the parameter ranges studied: $0.005 \leq Oh \leq 0.02$, $0.25 \leq C \leq 1$, $1 \leq L \leq 10$ and $0 \leq \alpha \leq 40°$. (b) A short tube ($L = 1.5$) fails to produce drop ejections under identical conditions to Fig. 5.4, where a longer tube ($L = 5$) does produce ejection. The jet reaches maximum length at $t^* = 1.07$ and then retracts.

natural to use it to account for the total amount of kinetic energy prior to jet formation. Fig. 5.7 plots the outcome of jet breakup against two parameters, We and L_e, where L_e has been made dimensionless by R. The overlaps in the We plot (Fig. 5.6a) have now been sorted out by L_e. This plot suggests the following criterion for predicting drop formation in auto-ejection:

$$N = \begin{cases} 0 & \text{if } We < 3.4f(L_e) \\ 1 & \text{if } 3f(L_e) < We < 5.5f(L_e) \\ 2 & \text{if } We > 5.5f(L_e) \end{cases} \tag{5.8}$$

where $f(L_e) = 1 + 0.8/L_e$. For the range of parameters tested here, ejection of 3 and more droplets has been observed mainly for large contraction angles, which produce a different flow regime to be considered in §5.4.3. Thus we do not include these cases here.

A few remarks about this criterion seem in order. First, the criterion is general as it encompasses almost the entire parameter ranges explored in our simulations. The material and geometric parameters of the problem have been included through We and L_e. The only exception is large contraction angles α that induce new flow patterns. This is to be dealt with separately

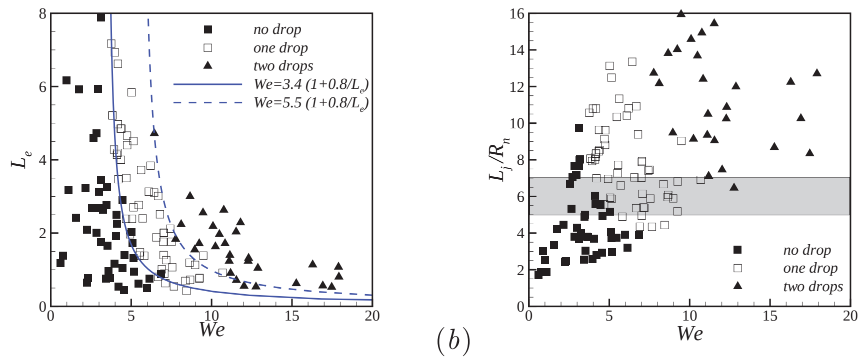

(a) (b)

Figure 5.7: (a) Criterion for self-ejection: number of droplets plotted as a function of We and the effective length L_e of equation (5.5). The three outcomes are demarcated by $We = 3.4(1+0.8/L_e$ and $We = 5.5(1+0.8/L_e)$, shown as the solid and dashed curves, respectively. (b) The gray band, representing $5 \leq L_j/R_n \leq 7$ for the jet length of equation (5.9), indicates a rough threshold for auto-ejection.

in §5.4.3. Second, the auto-ejection criterion is in terms of We and L_e, and does no explicitly account for the jet dynamics outside the nozzle, including the process of end-pinching. This is because the later dynamics are in principle dictated by these two control parameters. More specifically, We indicates the instantaneous upward momentum of the liquid column before a jet is produced, and L_e governs how that momentum decays in time (cf. eqution 5.6). Taken together, they determine the ultimate length of the jet that can be produced, which in turn determines whether end-pinching occurs and how many drops result. Equating the kinetic energy and meniscus surface energy at $t^* = 0$ to the surface energy of a cylindrical jet of radius R_n, $\frac{\pi}{2}R_n^2 \rho L_e V_e^2 + 2\pi R_n^2 \sigma = 2\pi R_n L_j \sigma$, we estimate the eventual length of the jet L_j once the kinetic energy has been completely converted to surface energy:

$$L_j = \frac{We}{4} L_e + R_n. \tag{5.9}$$

Now the numerical results of Fig. 5.7(a) can be reinterpreted in terms of L_j in Fig. 5.7(b). Roughly speaking, the transition from non-ejection to ejection occurs over the range of $5 \leq L_j/R_n \leq 7$. This coincides with the critical jet length that is determined for end-pinching on a initially stationary filament, $L_j/R_n = 6 \pm 1$ [14]. Thus L_j provides a connection between auto-ejection, in which the mass flux at the nozzle exit varies in time, and end-pinching

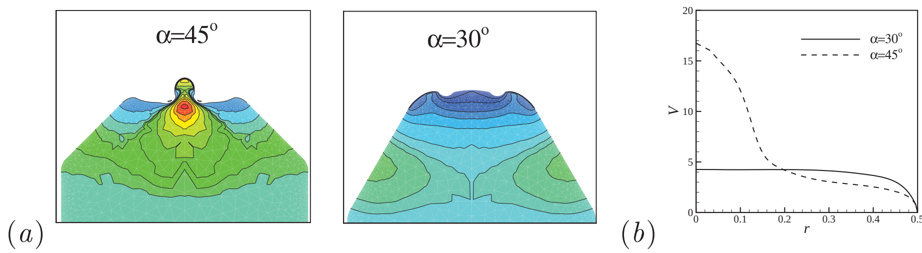

Figure 5.8: (a) Pressure field inside nozzles with $\alpha = 45°$ and $\alpha = 30°$ when jet starts protruding from the nozzle exit. There is a two-dimensional pressure filed with a high pressure region around the centreline for the nozzle with $\alpha = 45°$. (b) Comparison of the axial velocity profile at the nozzle exit between $\alpha = 30°$ and $\alpha = 45°$.

on a stationary filament where that flux is nil. The correspondence is not perfect, of course, since our jet shape can differ considerably from a perfect cylinder. At small Weber numbers, the strong capillary force makes the shape of the jet more spherical and hence increases the critical value of L_j. At high Weber numbers, the decaying velocity field at the exit produces a conical jet shape with a tapering tip. This amounts to an effectively thinner jet diameter, and consequently a smaller critical aspect ratio L_j for breakup. Still, the criterion of equation (5.8) is somewhat unsatisfactory in that it is expressed in terms of We based on the instantaneous velocity V_e, which is not one of the material or geometric parameters but a complex function of them. We have found no straightforward way to model V_e. This is because the acceleration of the meniscus in the nozzle depends on the dynamic contact angle θ_d, which depends on the meniscus velocity in turn (cf. Fig. 5.3). Thus, we have to content ourselves for the moment with an ejection criterion in terms of an instantaneous Weber number.

The criterion appears consistent with the experimental data of [88]. These data were presented in terms of a Weber number at the exit, similar to our We except that the local velocity was estimated using scaling arguments. Similar to our Fig. 5.6, different outcomes overlap considerably in terms of We values. Non-ejection was observed for We from around 2 up to nearly 20. The ejection of 1 or 2 droplets occurred for $6 < We < 20$, while three or more drops were seen for We above 10. Since the geometric parameters were not reported for the individual data points, we are unable to compute L_e and use it to untangle the data as we have done in Fig. 5.7. Thus, we can only observe that the experimental data suggest threshold We

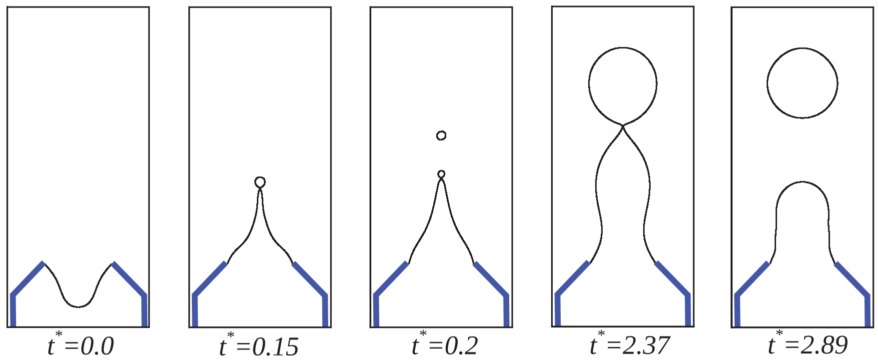

(*a*) (*b*) (*c*) (*d*) (*e*)

Figure 5.9: The regime of rapid ejection at contraction angle $\alpha = 45°$, other conditions being identical to those in Fig. 5.4. (a) $t^* = 0$; (b) ejection of the first drop at $t^* = 0.15$; (c) ejection of the second drop at $t^* = 0.2$; (d) ejection of the third drop at $t^* = 2.37$. (e) retraction of the filament.

values that are consistent with our results in Fig. 5.7.

Finally, the auto-ejection criterion makes an interesting prediction about the possibility of auto-ejection in a straight capillary tube. The maximum meniscus velocity in a straight capillary tube is the capillary-inertial velocity v_{ci} (equation 5.1), which yields a Weber number $We = 2\cos\theta \leq 2$. This is smaller than the minimum We for auto-ejection $We = 3.4f(L_e) > 3.4$. Thus, auto-ejection cannot occur in straight tubes, as has been suggested by empirical observations [70, 88].

5.4.3 Rapid ejection and air entrapment

This subsection deals with two new flow regimes encountered at large values of the contraction angle α. In constructing the pinch-off criterion, we have encoded all geometric effects into L_e. The contraction induces an inward radial flow, one consequence of which is to accelerate the average velocity of the liquid and increase the total kinetic energy. Using a one-dimensional plug flow assumption, we have represented the acceleration effect in L_e. For larger contraction angles, however, the two-dimensional nature of the flow becomes important, and the radial flow tends to modify the meniscus shape and the dynamic contact angle, thus producing new regimes of interfacial breakup. As a baseline, we take the simulation depicted in Fig. 5.4 at contraction angle $\alpha = 30°$. Note that when the contact line reaches the exit (point e), the meniscus as a whole arrives at the exit as well, with a more or less flat interface and uniform velocity profile. Subsequently, a more or less cylindrical jet is formed (point g), which grows to a maximum length around $5R_n$ before end-pinching produces a single large droplet. Considering this baseline scenario as "regular ejection", we encounter two new regimes at higher α, termed *rapid ejection* and *air entrapment*.

Rapid ejection is illustrated in Fig. 5.9 for $\alpha = 45°$. The stronger contraction leads to faster acceleration of the contact line speed, as well as a larger and increasing contact angle. Since capillarity cannot keep up with the rapid contact line movement, the meniscus deviates markedly from a spherical shape, and a deep depression forms in the center (Fig. 5.9(a), $t^* = 0$). Afterwards, the strong radial flow converges toward the center, while surface tension lifts the meniscus rapidly. The pressure field inside the nozzle slightly after jet's protrusion from nozzle exit is shown in Fig. 5.8(a). These two effects conspire to produce a highly non-uniform velocity profile when the meniscus as a whole reaches the exit. As shown in Fig. 5.8(b), the centerline velocity is much higher than the average velocity V_n for $\alpha = 45°$, as compared with the baseline case of $\alpha = 30°$. As a result, the first drop is ejected quickly at $t^* = 0.15$, with drop radius $r = 0.07$ and velocity $v = 14.8$. This is followed by a second small drop ($r = 0.046$, $v = 6.9$) at $t^* = 0.20$, and a much larger third one ($r = 0.54$, $v = 0.06$) after a much longer interval at $t^* = 2.37$. In contrast, the baseline case has its first and only ejection at $t^* = 1.66$, producing a much larger and slower drop ($r = 0.61$, $v = 1.02$). After the third drop, the jet retracts. In view of the rapid ejection of high-speed droplets, higher α may help induce auto-ejection under normal-gravity conditions. Indeed, the ancillary video of [87] depicts auto-ejection under normal gravity using a large contraction angle $\alpha = 50°$. We have carried out a limited exploration of such scenarios, and an example is depicted in Fig. 5.10 for Bond number $Bo = \rho R^2 g/\sigma = 0.4$ at $\alpha = 50°$. After the ejection of one droplet, the jet grows a bulb at the tip while forming a neck at the base ($t^* = 0.42$). Shortly afterwards, the neck pinches in and the bulb detaches, producing two drops of disparate size ($t^* = 0.5$). Under the same conditions, contraction angles below 40° do not produce auto-ejection at all. It is thanks to the stronger radial flow that a thin jet forms and breaks up into droplets.

Air entrapment occurs at an even larger contraction angle of $\alpha = 55°$ (Fig. 5.11). At $t^* = 0$, the interface forms a depression as in the rapid-ejection regime. Subsequently, however, the radial flow is so strong as to cause the depression to narrow and deepen, producing an air finger. At

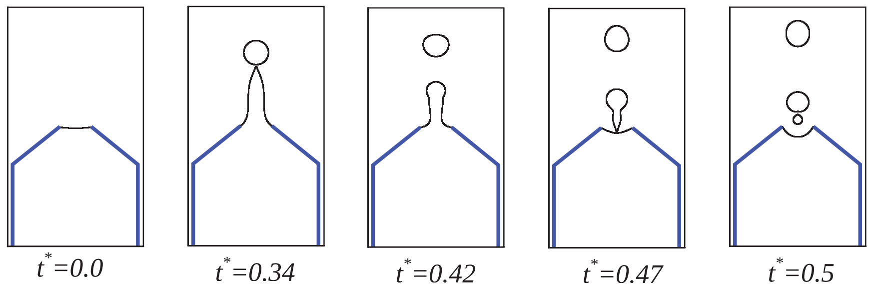

Figure 5.10: Auto-ejection under gravity for large contraction angle. $Bo = 0.4$, $Oh = 0.01$, $\alpha = 50°$, $C = 0.25$, $L = 2$. After ejecting a single droplet at $t^* = 0.34$, the jet pinches off at its base ($t^* = 0.47$), and later breaks up into two more drops ($t^* = 0.5$).

$t^* = 0.079$, the neck of the air finger pinches off, entrapping a bubble in the liquid. Given the relatively short length of the air finger, the pinch-off is dynamically driven by the inward liquid flow rather than interfacial tension as in Rayleigh-Plateau instability. After this, the strong momentum of the liquid continues to propel the jet forward, much like the later stage of Fig. 5.9. This leads to the ejection of a large drop ($r = 0.49$, $v = 0.71$) at $t^* = 1.68$. Eventually the jet retracts. Experimentally, [87] demonstrated the possibility of the air entrapment regime under normal gravity at $\alpha \approx 50°$ and $Oh = 0.005$. This provides direct evidence for this unusual flow regime. To conclude the investigation of the contraction angle α, we note that auto-ejection favors an intermediate range of α values. Too gentle a contraction does not provide sufficient flow focusing to produce a long jet. Too abrupt a contraction stifles the upward momentum of the liquid column, again suppressing drop ejection.

5.4.4 Contact line depinning at nozzle lip

So far, we have assumed the nozzle exit to be a horizontal surface of width W_l that is completely non-wettable by the liquid ($\theta_l = 180°$). Thus, the contact line is pinned at the inner corner of the lip. Under certain experimental conditions, the contact line has been observed to depin and move outward [87]. This effectively broadens the base of the jet and changes the outcome of drop ejection [2]. This has motivated us to relax the pinning condition by imposing a smaller θ_l so that the effect of contact line depinning can be

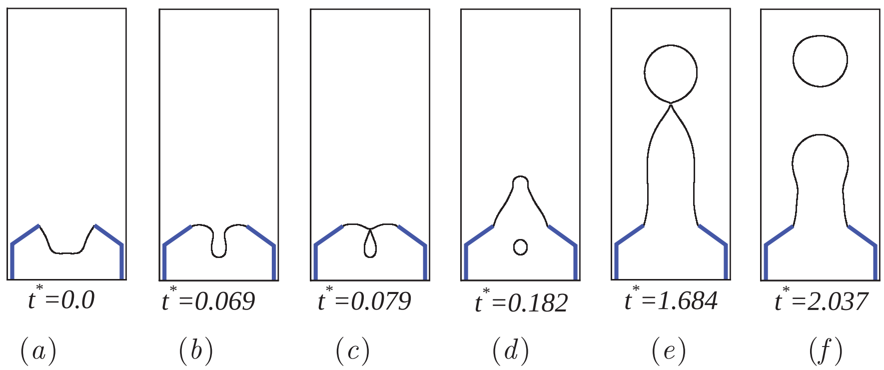

Figure 5.11: Air entrapment at contraction angle $\alpha = 55°$, other conditions being identical to those in Fig. 5.4. (a) $t^* = 0$; (b) formation of air finger at $t^* = 0.069$; (c) pinch-off of the air bubble at $t^* = 0.079$; (d) jet continues out of the nozzle (e) droplet pinch-off at $t^* = 1.684$ after bubble entrapment. Air bubble disappears due to diffusion of numerical (f) filament retraction.

investigated.

Fig. 5.12 depicts the effect of contact line depinning by tracking the position of the centreline of interface in time for several values of θ_l. As the jet emanates from the nozzle, the interfacial slope never exceeds 90° relative to the upper surface of the lip. Thus, for $\theta_l \geq 90°$, the contact line remains pinned at the inner corner of the lip and θ_l has no effect. These cases are represented by the $\theta_l = 90°$ curve in Fig. 5.12(a). The geometric and physical conditions for these runs correspond to $We = 6.9$ and $L_e = 1.46$, and thus auto-ejection of a single drop occurs according to Fig. 5.7. As θ_l reduces to 80° and 70°, the contact line depins and moves outward. This hampers the lengthening of the jet and delays the pinch-off. The drop produced is also somewhat larger. At the point of pinch-off, the contact line is somewhere on the flat part of the upper surface, not having reached the outer corner. For $\theta_l \leq 60°$, the length of the jet is further stunted and drop ejection is completely suppressed. For these cases, the contact line reaches the outer edge of the lip and stays pinned there, at least until the jet retracts.

Fig. 5.12(b) analyzes the suppression of drop ejection for $\theta_l = 45°$. Depinning of the contact line takes place at point a when the interface makes an angle of 45° with respect to the upper surface of the exit. After de-pinning, the contact line moves radially outward, broadening the base of the jet. This

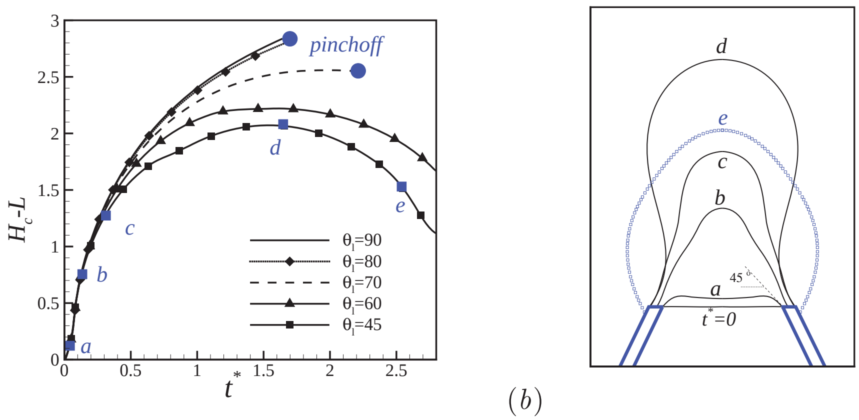

(a) (b)

Figure 5.12: (a) Effect of contact line depinning on the growth of the jet and drop ejection. The ordinate is the length of the jet measured from the exit of the nozzle, and the abscissa is time starting from the moment of the contact line reaching the inner corner of the lip. Drop pinch-off is indicated by a round dot. The width of the upper surface is fixed at $W_l = 0.25R_n$, and θ_l is the contact angle on the upper surface. The other parameters of the simulation are $C = 0.5$, $\alpha = 30°$, $L = 4$, $\theta = 0$ (on the inner surface) and $Oh = 0.01$. (b) Snapshots of the interface for $\theta_l = 45°$ at points marked on the curve.

reduces the upward liquid velocity through mass conservation. Moreover, the curvature of the meniscus is moderated (point b), resulting in a lower capillary pressure at the base of the jet. Both effects conspire to restrain the lengthening of the jet. The contact line reaches the outer corner of the lip at point c, and the jet length peaks at point d some time later. This maximum jet length, at $2R = 4R_n$ (Fig. 5.12a), is about 25% shorter than the case without contact line depinning ($\theta_l \geq 90°$). It is too short for drop ejection (cf. Fig. 5.7b). Thus, the jet retracts and flattens afterwards, driving the contact line past the outer corner, producing the nearly spherical interface of point e.

Insofar as the contact line becomes pinned at the outer corner of the lip during the growth phase of the jet, the width W_l of the lip should also affect the jet behavior. For a fixed $\theta_l = 45°$, we have examined the effect of increasing W_l from $0.05R_n$ to $2R_n$. As expected, a wider lip broadens the base of the jet, inhibits the lengthening of the jet, and suppresses the potential for drop ejection.

5.5 Summary and conclusions

As far as we know, this study represents the first numerical computation of the process of auto-ejection. In interpreting the numerical results, we have also developed simple models to describe various aspects of the process. The parameter range captures most of the experimental conditions, and we reproduce all the salient features of the experimental observations. The main results of the study can be summarized as follows.

(*a*) The meniscus quickly attains the capillary-inertial regime in the straight tube, and advances with a mostly constant velocity until it enters the contraction in the nozzle, where it accelerates. The dynamic contact angle increases with the meniscus speed. Viscosity has a negligible role in the entire process.

(*b*) With the contact line pinned at the inner corner of the exit, a jet issues into the ambient air. The lengthening of the jet is accompanied by deceleration of the liquid column inside the tube, with kinetic energy being converted into surface energy. An energy balance model captures the temporal decay of the liquid velocity at the nozzle quite accurately. This rate of decay is dictated by an effective length that embodies the geometric features of of the tube-nozzle combination.

(*c*) A two-parameter criterion for auto-ejection of droplets is developed using the instantaneous Weber number when the contact first arrives at the nozzle exit and the effective length. Together they determine the length of the jet that may be produced when the available kinetic energy is converted into surface energy. This critical length agrees with prior studies of end-pinching on an initially stationary filament, thus demonstrating our criterion as being rooted in essentially the same hydrodynamics.

(*d*) With increasing contraction angle, we predict new regimes of rapid ejection of multiple drops and air bubble entrapment. When the contraction is too mild, auto-ejection is suppressed. In particular, auto-ejection is impossible in a straight tube.

(*e*) To the extent that comparisons can be made, the numerical results agree with experimental observations.

One limitation of the study is that the criterion for auto-ejection is given in terms of an instantaneous Weber number, rather than in terms of the material and geometric parameters. We attempted to model the instantaneous velocity at the nozzle in terms of these parameters, with little success. As compared with other microfluidic drop-forming procedures, auto-ejection is unique in that it involves no external force or flux, and is entirely autonomous. From this standpoint, it will be desirable to devote future work to refining the current criterion into one expressed in the geometric and material parameters.

Chapter 6

Conclusions and Recommendations

In this thesis, the Cahn-Hilliard diffuse-interface model is used to numerically study three interfacial dynamic problems. The diffusive interface removes the contact line singularity and singular topological events during the pinch-off and coalescence. In addition, the finite thickness of the interface with the energy-based formulation of the Cahn-Hilliard model enables us to capture the contact line dynamics and interfacial tension more naturally. In the following, a summary of key findings for each studied problem is presented. Then the significance and limitations are discussed. Finally recommendation for future works are made.

6.1 Summary of key findings

6.1.1 Capillary breakup of a liquid torus

The capillary breakup of a Newtonian liquid torus suspended in a surrounding Newtonian liquid is studied. Starting from an externally imposed sinusoidal disturbance, the initial stage of the growth is linear and the additional curvature of the torus around its axis inhibits the growth of the imposed wavelength compared to its counterpart on the straight filament. The contraction of the torus toward its center amplifies the disturbance growth by producing an external flow field.

The final shape of the torus breakup and the number of produced droplets are an outcome of the competition between the contraction of the torus and capillary instability. This competition is controlled by three parameters which are torus-to-medium viscosity ratio, torus aspect ratio, and initial amplitude of the disturbance. A large aspect ratio for the torus lengthens the shrinkage time. In addition, a large aspect ratio increases the disturbance growth by reducing the axial curvature. Therefore a large aspect ratio favors the capillary pinch-off mechanism. The torus-to-medium viscosity ratio is important for both processes. Higher viscosity ratios make the shrinkage faster and increase the growth rate of the disturbance. The dependence of shrinkage on viscosity ratio is stronger. Therefore, increasing the viscosity ratio favors the shrinkage mechanism. Increasing the initial amplitude of the disturbance shortens the time for the capillary pinch-off.

6.1.2 Wicking flow through microchannels

Wicking flow is a key mechanism for flow movement inside the complex micropore geometries of porous media. The dynamics of a meniscus in a pore is dependent on its shape, connectivity with other pores, liquid-solid, liquid-air, and solid-air interfacial tensions, and flow properties. For inertia-less flows, an axisymmetric contraction, expansion and their combination are used to study the effect of pore shape on the meniscus dynamics. It is shown that the interface moves through a contraction or an expansion through three main steps: shape adjustment at inward corners, movement of spherical meniscus, and pinning at outward corners. At inward corners, first the contact line moves in and rotates. The tendency of the meniscus to keep a spherical profile pushes the center of the meniscus downward. The diffusive nature of the interface enables the meniscus to negotiate the large contraction angles at inward corners, which presents a singularity for a sharp interface formulation. Then the meniscus moves in with nearly a spherical shape until it reaches the end of the contraction. At outward corners, the contact line gets pinned and the meniscus center moves up to minimize its surface energy until it makes enough angle with the next section to depin and move forward. For large contraction angles, dynamics of meniscus at inward corner can change the passage time considerably. In expansion geometries, due to a usually slow meniscus movement, neglecting the meniscus dynamic at the corner does not affect the passage time considerably.

A simple 2D Y-branching geometry is used to study the connectivity of pores. The flow trajectory depends on the capillary forces in the branches as well as viscous dissipation inside the root channel. Counter-intuitively, flow moves into the narrower channels if there is large dissipation inside the root conduit.

6.1.3 Auto-ejection of liquid jets and drops from capillary tubes

Auto-ejection is studied for low Ohnesorge number liquids which perfectly wet the solid in a zero-gravity environment with negligible surrounding air effects.

The dynamics of the meniscus inside the tube and the nozzle are studied. It is shown that the effect of viscosity is negligible and the meniscus dynamics can be understood qualitatively by assuming plug flow. Inside the nozzle, the interaction of accelerating flow field and contact line dynamics produces complex meniscus dynamics which is carefully analyzed.

A two-parameter ejection criterion is developed. It is shown that the ejection criterion depends on the momentum of the ejecting liquid and its decay rate. The momentum of the ejecting liquid is quantified in terms of the Weber number at the nozzle exit when the meniscus first gets pinned there. Its decay rate is dependent on the kinetic energy. Using a one dimensional flow inside the tube and nozzle, and sink flow inside the reservoir, it is possible to relate the velocity at each point inside tube-nozzle reservoir combination to the velocity at the nozzle exit. Then total kinetic energy can be expressed in terms of an effective length and velocity at the nozzle exit. It is shown that such an effective length is important in categorizing different ejection regimes. The importance of the effective length is further shown by relating the auto-ejection data to the critical aspect ratio for breakup of stationary filaments during the retraction. It is shown that the effective length is related to the length of the jet that can be produced by converting the liquid kinetic energy into surface energy.

To obtain the effective length one dimensional plug flow assumption is used inside the tube and nozzle. Such an assumption is not valid for high contraction angles where the strong radial flow produces two-dimensional flow inside the nozzle. It is shown that at large contraction angles, a strong radial flow produces a highly curved meniscus inside the nozzle. This leads to two new regimes, rapid ejection and air entrapment, with increasing contraction angles.

6.2 Significance and limitations

Nowadays due to miniaturization and micro-engineering, interface dynamic and its interaction with bulk flow take on increasing scientific and practical importance. In auto-ejection under normal gravity, for example, the detailed information about the shape adjustment stage of meniscus movement through contractions can be used to promote droplet ejection.

Information on contact line dynamics is difficult to gain through experimental and numerical studies. Experiments always face unwanted factors such as surface roughness and heterogeneity and visualization problems. Numerically, there is a singularity in macroscopic equations for the contact line movement for which there is at present no satisfactory model. The Cahn-Hilliard diffuse-interface method provides a physically motivated formulation to investigate contact line dynamics. By tuning its parameters for a certain fluid-solid combination, it is possible to study the dynamics which are usually hard to capture. An example is the variation of the dynamic contact angle inside the nozzle for the auto-ejection problem.

Understanding the pore scale interfacial dynamics is the building block for developing better models for porous media flow. Such understanding can be used to design more efficient gas diffusion layers for fuel cells. Two main features of pores are their non-uniform cross section and connectivity. The performed research helps to understand the interface dynamics in these two geometries.

Capillary instability plays a main role in most of the droplet production mechanisms. Knowledge of capillary instability is further extended by taking into account the effect of filament curvature and compressive flow field. In addition, liquid rings are unstable configurations and will eventually contract onto themselves or breakup into droplets. Therefore, the simplified two times-scale model will give an insight into the fate of the torus.

We have compared our numerical simulations with experimental and theoretical results. There is a good agreement between physical observations and numerical results which further demonstrates the ability of the Cahn-Hilliard model to produce physically meaningful results.

There are also limitation for this research, which we summarize below:

- Computational limitation. Realization of the sharp interface limit is computationally very expensive. This becomes a more severe issue for three dimensional interfaces and when there are disparate length scales in the problems. Besides, our AMPHI algorithm uses a fully implicit time-updating scheme. Although this improves stability, the computational cost in inverting the matrix is high. More efficient split algorithms might help alleviate the problem.

- Limitation of the Cahn-Hilliard contact line model. The phenomenological nature of the contact line model implies that model parameters need to be determined from experimental data, which are not always available for the geometry and materials required. In addition, resolving the diffusion length which is around six orders of magnitude smaller than the bulk length scale is numerically challenging.

6.2.1 Recommendations for future work

The current work can be further extended in certain aspects. In the analysis of the torus instability, we have not considered the effect of non-symmetric disturbances. In reality the geometry of the torus is not a prefect ring and it can have defects on its surface. How such defects modify the breakup of liquid torus can be studied. In addition, we showed that the initially fastest mode may not proceed to the end. How a combination of different modes grow on the torus and how they morph into each other needs to be studied. It is also interesting to study the capillary instability of the ring in the presence of gravity where thick and thin parts of the disturbed torus will experience different buoyancy forces and the growth of the disturbance will be affected.

For wicking flow one can experimentally study the flow branching and also extend it to more realistic geometries for pore-connectivity, including 3D branches and networks. Such studies will provide a benchmark for the popular pore-network models. In addition, it can be extended to include the effect of gravity on meniscus dynamics in Y-branches and also through contraction or expansion.

For auto-ejection, it will be desirable to devote future work to refining the current criterion into one expressed in the geometric and material parameters. In addition, one can explore the dependency of droplet size on geometric and solid-fluid properties. We have done a limited test for a 1-g condition, which can be explored in more detail. Finally, the modeling of the dynamic contact angle in the Cahn-Hilliard model needs to be studied more carefully, especially in regards to the energy dissipation at the contact line.

Bibliography

[1] M. Ahmadlouydarab, Z.-S. Liu, and J. J. Feng. Interfacial flows in corrugated microchannels: flow regimes, transitions and hysteresis. *Int. J. Multiphase Flow*, 37:1266–1276, 2011.

[2] B. Ambravaneswaran, H. J. Subramani, S. D. Phillips, and O. A. Basaran. Dripping-jetting transitions in a dripping faucet. *Phys. Rev. Lett.*, 93:34501, 2004.

[3] B. Ambravaneswaran, E. D. Wilkes, and O. A. Basaran. Drop formation from a capillary tube: Comparison of one-dimensional and two-dimensional analyses and occurrence of satellite drops. *Phys. Fluids*, 14:2606–2621, 2002.

[4] S. L. Anna, N. Bontoux, and H. A. Stone. Formation of dispersions using 'flow focusing' in microchannels. *Appl. Phys. Lett.*, 82:364–366, 2003.

[5] A. Antkowiak, N. Bremond, J. Duplat, S. Le Dizès, and E. Villermaux. Cavity jets. *Phys. Fluids*, 19(9):091112–091112, 2007.

[6] H. Benkreira and M. I. Khan. Air entrainment in dip coating under reduced air pressures. *Chemical Engineering Science*, 63(2):448 – 459, 2008.

[7] G. Blankenstein and U. D. Larsen. Modular concept of a laboratory on a chip for chemical and biochemical analysis. *Biosens. Bioelectron.*, 13:427–438, 1998.

[8] C. H. Bosanquet. On the flow of liquids into capillary tubes. *Philos. Mag. Ser. 6*, 45:525–531, 1923.

[9] J. B. Bostwick and P. H. Steen. Stability of constrained cylindrical interfaces and the torus lift of Plateau-Rayleigh. *J. Fluid Mech.*, 647:201–219, 2010.

[10] S. Bouaidat, O. Hansen, H. Bruus, C. Berendsen, N. K. Bau-Madsen, P. Thomsen, A. Wolff, and J. Jonsmann. Surface-directed capillary system; theory, experiments and applications. *Lab Chip*, 5:827–836, 2005.

[11] M. Bracke, F. De Voeght, and P. Joos. The kinetics of wetting: the dynamic contact angle. In *Trends in Colloid and Interface Science III*, pages 142–149. Springer, 1989.

[12] G. Caginalp and X. Chen. Convergence of the phase field model to its sharp interface limits. *Euro. J. Appl. Math.*, 9:417–445, 1998.

[13] J. W. Cahn and J. E. Hilliard. Free energy of a non-uniform system. Part I: interfacial free energy. *J. Chem. Phys.*, 28:258–267, 1958.

[14] A. Castrejón-Pita, J. Castrejón-Pita, and I. Hutchings. Breakup of liquid filaments. *Phys. Rev. Lett.*, 108(7), 2012.

[15] J. R. Castrejón-Pita, A. A. Castrejón-Pita, E. J. Hinch, J. R. Lister, and I. M. Hutchings. Self-similar breakup of near-inviscid liquids. *Phys. Rev. E*, 86(1):015301, 2012.

[16] R. Chein and S. H. Tsai. Microfluidic flow switching design using volume of fluid model. *Biomed. Microdevices*, 6:81–90, 2004.

[17] J. M. Chen, P. C. Huang, and M. G. Lin. Analysis and experiment of capillary valves for microfluidics on a rotating disk. *Microfluid. Nanofluid.*, 4:427–437, 2008.

[18] I. Cohen, M. P. Brenner, J. Eggers, and S. R. Nagel. Two fluid drop snap-off problem: Experiments and theory. *Phys. Rev. Lett.*, 83:1147–1150, 1999.

[19] O. Cohu and H. Benkreira. Air entrainment in angled dip coating. *Chemical Engineering Science*, 53(3):533 – 540, 1998.

[20] R. G. Cox. The dynamics of the spreading of liquids on a solid surface. Part 1: Viscous flow. *J. Fluid Mech.*, 168:169–194, 1986.

[21] H. Czachor. Modeling the effect of pore structure and wetting angles on capillary rise in soils having different wettabilities. *J. Hydrol.*, 328:604–613, 2006.

[22] N. Djilali. Computational modelling of polymer electrolyte membrane (PEM) fuel cells: Challenges and opportunities. *Energy*, 32:269–280, 2007.

[23] M. Dreyer, A. Delgado, and H. J. Rath. Capillary rise of liquid between parallel plates under microgravity. *J. Colloid Interface Sci.*, 163:158–168, 1994.

[24] J. Eggers and E. Villermaux. Physics of liquid jets. *Rep. Prog. Phys.*, 71:036601, 2008.

[25] D. Erickson, D. Li, and C. B. Park. Numerical simulation of the capillary driven flows in non-uniform cross sectional capillaries. *J. Colloid Interface Sci.*, 250:422–430, 2002.

[26] L. A. Freitag and C. Ollivier-Gooch. Tetrahedral mesh improvement using swapping and smoothing. *Int. J. Numer. Meth. Engng.*, 40:3979–4002, Jul 1997.

[27] P. Gao and J. J. Feng. Enhanced slip on a patterned substrate due to depinning of contact line. *Phys. Fluids*, 21:102102, 2009.

[28] P. Gao and J. J. Feng. A numerical investigation of the propulsion of water walkers. *J. Fluid Mech.*, 668:363–383, 2011.

[29] P. Gao and J. J. Feng. Spreading and breakup of a compound drop on a partially wetting substrate. *J. Fluid Mech.*, 682:415–433, 2011.

[30] S. Gekle and J. M. Gordillo. Generation and breakup of worthington jets after cavity collapse. part 1. jet formation. *J. Fluid Mech.*, 663:293–330, 2010.

[31] T. Goldmann and J. Gonzalez. DNA-printing: utilization of a standard inkjet printer for the transfer of nucleic acids to solid supports. *Journal of biochemical and biophysical methods*, 42(3):105–110, 2000.

[32] D. A. Gomes. Stability of rotating liquid films. *Q. J. Mech. Appl. Math.*, 55:327–343, 2002.

[33] R. C. Goodknight, W. A. Klikoff, and I. Fatt. Non-steady-state fluid flow and diffusion in porous media containing dead-end pore volume. *J. Phys. Chem.*, 64(9):1162–1168, 1960.

[34] J. M. Gordillo and S. Gekle. Generation and breakup of worthington jets after cavity collapse. part 2. tip breakup of stretched jets. *J. Fluid Mech.*, 663:331–346, 2010.

[35] G. J. Gutierrez, A. Medina, and F. J. Higuera. Equilibrium height of a liquid in a gap between corrugated walls under spontaneous capillary penetration. *J. Colloid Interface Sci.*, 338:519–522, 2009.

[36] J. Ha and L. G. Leal. An experimental study of drop deformation and breakup in extensional flow at high capillary number. *Phys. Fluids*, 13:1568, 2001.

[37] S. Herminghaus, M. Brinkmann, and R. Seemann. Wetting and dewetting of complex surface geometries. *Annu. Rev. Mater. Res.*, 38:101–121, 2008.

[38] R. L. Hoffman. A study of the advancing interface. I. Interface shape in liquid-gas systems. *J. Colloid Interface Sci.*, 50:228–241, 1975.

[39] D. Jacqmin. Calculation of two-phase Navier-Stokes flows using phase-field modeling. *J. Comput. Phys.*, 155:96–127, 1999.

[40] D. Jacqumin. Contact-line dynamics of a diffuse fluid interface. *J. Fluid Mech.*, 402:57–67, 2000.

[41] T.-S. Jiang, O.-H. Soo-Gun, and J. C. Slattery. Correlation for dynamic contact angle. *J. Colloid Interface Sci.*, 69, 1979.

[42] P. Joos, P. Van Remoortere, and M. Bracke. The kinetics of wetting in a capillary. *J. Colloid Interface Sci.*, 136:189–197, 1990.

[43] D. L. Keij, K. G. Winkels, H. Castelijns, M. Riepen, and J. H. Snoeijer. Bubble formation during the collision of a sessile drop with a meniscus. *Phys. Fluids*, 25(8):082005, 2013.

[44] G. B. Lee, C. I. Hung, B. J. Ke, G. R. Huang, and B. H. Hwei. Micromachined pre-focused 1×N flow switches for continuous sample injection. *J. Micromech. Microeng.*, 11:567, 2001.

[45] S. Leib and M. Goldstein. Convective and absolute instability of a viscous liquid jet. *Phys. Fluids*, 29, 1986.

[46] G. Lin and T. V. Nguyen. Effect of thickness and hydrophobic polymer content of the gas diffusion layer on electrode flooding level in a PEMFC. *J. Electrochem. Soc.*, 152:A1942–A1948, 2005.

[47] W. W. Liou, Y. Peng, and P. E. Parker. Analytical modeling of capillary flow in tubes of nonuniform cross section. *J. Colloid Interface Sci.*, 333:389–399, 2009.

[48] S. Litster, D. Sinton, and N. Djilali. Ex situ visualization of liquid water transport in pem fuel cell gas diffusion layers. *J. Power Sources*, 154:95–105, 2006.

[49] R. Lucas. Ueber das zeitgesetz des kapillaren aufstiegs von flüssigkeiten. *Kolloid Z.*, 23:15–22, 1918.

[50] J. D. McGraw, J. Li, D. L. Tran, A.-C. Shi, and K. Dalnoki-Veress. Plateau-Rayleigh instability in a torus: formation and breakup of a polymer ring. *Soft Matter*, 6:1258–1262, 2010.

[51] H. Mehrabian and J. J. Feng. Wicking flow through microchannels. *Phys. Fluids*, 23:122108, 2011.

[52] T. Mikami, R. G. Cox, and S. G. Mason. Breakup of extending liquid threads. *Int. J. Multiphase Flow*, 2:113–138, 1975.

[53] T. Mikami and S. G. Mason. The capillary break-up of a binary liquid column inside a tube. *Can. J. Chem. Eng.*, 53:372–377, 1975.

[54] J. H. Nam and M. Kaviany. Effective diffusivity and water-saturation distribution in single- and two-layer pemfc diffusion medium. *Int. J. Heat Mass Transfer*, 46:4595–4611, 2003.

[55] T. D. Nguyen, M. Fuentes-Cabrera, J. D. Fowlkes, J. A. Diez, A. G. González, L. Kondic, and P. D. Rack. Competition between collapse and breakup in nanometer-sized thin rings using molecular dynamics and continuum modeling. *Langmuir*, 28:13960–13967, 2012.

[56] P. K. Notz and O. A. Basaran. Dynamics and breakup of a contracting liquid filament. *J. Fluid Mech.*, 512(1):223–256, 2004.

[57] E. Pairam and A. Fernández-Nieves. Generation and stability of toroidal droplets in a viscous liquid. *Phys. Rev. Lett.*, 102:234501, Jun 2009.

[58] G.-G. Park, Y.-J. Sohn, T.-H. Yang, Y.-G. Yoon, W.-Y. Lee, and C.-S. Kim. Effect of PTFE contents in the gas diffusion media on the performance of PEMFC. *J. Power Sources*, 131:182–187, 2004.

[59] U. Pasaogullari and C. Y. Wang. Liquid water transport in gas diffusion layer of polymer electrolyte fuel cells. *J. Electrochem. Soc.*, 151:A399–A406, 2004.

[60] D. Patro, S. B., and V. Jayaram. Flow kinetics in porous ceramics: Understanding with non-uniform capillary models. *J. Am. Ceram. Soc.*, 90:3040–3046, 2007.

[61] L. M. Pismen. Nonlocal diffuse interface theory of thin films and the moving contact line. *Phys. Rev. E*, 64:021603, Jul 2001.

[62] L. M. Pismen. Mesoscopic hydrodynamics of contact line motion. *Colloids Surf., A*, 206:11–30, 2002.

[63] A. Pizzi and K. L. Mittal. *Handbook of Adhesive Technology.* Marcel Dekker, New York, 2003.

[64] D. Quéré, É. Raphaël, and J. Ollitrault. Rebounds in a capillary tube. *Langmuir*, 15(10):3679–3682, 1999.

[65] L. Rayleigh. On the instability of jets. *Proc. Lond. Math. Soc.*, 10:4–13, 1878.

[66] M. Reyssat, L. Courbin, E. Reyssat, and H. A. Stone. Imbibition in geometries with axial variations. *J. Fluid Mech.*, 615:335–344, 2008.

[67] R. M. S. M. Schulkes. The contraction of liquid filaments. *J. Fluid Mech.*, 309:277–300, 1996.

[68] R. Sharma and D. S. Ross. Kinetics of liquid penetration into periodically constricted capillaries. *J. Chem. Soc., Faraday Trans.*, 87:619–624, 1991.

[69] J. Shen. Efficient spectral-Galerkin method. II. direct solvers of second and fourth order equations by using Chebyshev polynomials. *SIAM J. Sci. Comput.*, 16:74–87, 1995.

[70] R. Siegel. Transient capillary rise in reduced and zero-gravity fields. *J. Appl. Mech.*, 83:165–170, 1961.

[71] W. A. Sirignano and C. Mehring. Review of theory of distortion and disintegration of liquid streams. *Prog. Energy Combust. Sci.*, 26:609–655, 2000.

[72] M. Stange, M. E. Dreyer, and H. J. Rath. Capillary driven flow in circular cylindrical tubes. *Phys. Fluids*, 15:2587, 2003.

[73] T. L. Staples and D. G. Shaffer. Wicking flow in irregular capillaries. *Colloids Surf., A*, 204:339–350, 2002.

[74] H. A. Stone and L. G. Leal. Relaxation and breakup of an initially extended drop in an otherwise quiescent fluid. *J. Fluid Mech.*, 198:399–427, 1989.

[75] M. Switkes. Bubbles in immersion lithography. *Journal of vacuum science and technology. B Microelectronics processing and phenomena*, 23:217 – 236, 2005.

[76] J. Szekely, A. W. Neumann, and Y. K. Chuang. The rate of capillary oenetration and the applicability of the Washburn equation. *J. Colloid Interface Sci.*, 35:273–278, 1971.

[77] S. Takeuchi, P. Garstecki, D. B. Weibel, and G. M. Whitesides. An axisymmetric flow-focusing microfluidic device. *Adv. Mater.*, 17:1067–1072, 2005.

[78] T. Tanuma. Innovative hydrophilic microporous layers for cathode gas diffusion media. *J. Electrochem. Soc.*, 157(12):B1809–B1813, 2010.

[79] M. Tjahjadi, H. A. Stone, and J. M. Ottino. Satellite and subsatellite formation in capillary breakup. *J. Fluid Mech.*, 243:297–317, 1992.

[80] S. Tomotika. On the instability of a cylindrical thread of a viscous liquid surrounded by another viscous fluid. *Proc. R. Soc. London, Ser. A*, 150:322–337, 1935.

[81] S. Tomotika. Breaking up of a drop of viscous liquid immersed in another viscous fluid which is extending at a uniform rate. *Proc. R. Soc. London, Ser. A*, 153:302–318, 1936.

[82] A. Y. Tong and Z. Wang. Relaxation dynamics of a free elongated liquid ligament. *Phys. Fluids*, 19:092101, 2007.

[83] A. Umemura. Self-destabilizing mechanism of a laminar inviscid liquid jet issuing from a circular nozzle. *Phys. Rev. E*, 83(4):046307, 2011.

[84] A. S. Utada, E. Lorenceau, D. R. Link, P. D. Kaplan, H. A. Stone, and D. A. Weitz. Monodisperse double emulsions generated from a microcapillary device. *Science*, 308:537–541, 2005.

[85] E. W. Washburn. The dynamics of capillary flow. *Phys. Rev.*, 17:273–283, 1921.

[86] A. Wollman. Capillarity-driven droplet ejection. Master's thesis, Portland State University, USA, 2012.

[87] A. Wollman, T. Snyder, D. Pettit, and M. Weislogel. Spontaneous capillarity-driven droplet ejection. *arXiv:1209.3999*, 2012.

[88] A. Wollman and M. Weislogel. New investigations in capillary fluidics using a drop tower. *Exp. in Fluids*, 54(4):1–13, 2013.

[89] Y. Wu, J. D. Fowlkes, P. D. Rack, J. A. Diez, and L. Kondic. On the breakup of patterned nanoscale copper rings into droplets via pulsed-laser-induced dewetting: Competing liquid-phase instability and transport mechanisms. *Langmuir*, 26:11972–11979, 2010.

[90] Z.-N. Wu. Approximate critical Weber number for the breakup of an expanding torus. *Acta Mech.*, 166:231–239, 2003.

[91] Q. Xu and O. A. Basaran. Computational analysis of drop-on-demand drop formation. *Phys. Fluids*, 19:102111, 2007.

[92] Z. Yao and M. Bowick. The shrinking instability of toroidal liquid droplets in the Stokes flow regime. *Euro. Phys. J. E*, 34:1–6, 2011.

[93] P. Yue and J. J. Feng. Can diffuse-interface models quantitatively describe moving contact lines? *Eur. Phys. J - Spec. Top.*, 197:37–46, 2011.

[94] P. Yue and J. J. Feng. Wall energy relaxation in the Cahn-Hilliard model for moving contact lines. *Phys. Fluids*, 23:012106, 2011.

[95] P. Yue, C. Zhou, and J. J. Feng. A computational study of the coalescence between a drop and an interface in Newtonian and viscoelastic fluids. *Phys. Fluids*, 18:102102, 2006.

[96] P. Yue, C. Zhou, and J. J. Feng. Sharp interface limit of the cahn-hilliard model for moving contact lines. *J. Fluid Mech.*, 645:279–294, 2010.

[97] P. Yue, C. Zhou, J. J. Feng, C. F. Ollivier-Gooch, and H. H. Hu. Phase-field simulations of interfacial dynamics in viscoelastic fluids using finite elements with adaptive meshing. *J. Comput. Phys.*, 219:47–67, 2006.

[98] B. V. Zhmud, F. Tiberg, and K. Hallstensson. Dynamics of capillary rise. *J. Colloid Interface Sci.*, 228:263–269, 2000.

[99] C. Zhou, P. Yue, and J. J. Feng. Formation of simple and compound drops in microfluidic devices. *Phys. Fluids*, 18:092105, 2006.

[100] C. Zhou, P. Yue, J. J. Feng, C. F. Ollivier-Gooch, and H. H. Hu. 3D phase-field simulations of interfacial dynamics in Newtonian and viscoelastic fluids. *J. Comput. Phys.*, 229:498–511, 2010.

[101] D. Zhou, P. Yue, and J. J. Feng. Viscoelastic effects on drop deformation in a converging pipe flow. *J. Rheol.*, 52:469–487, 2008.

[102] M.-Y. Zhou and P. Sheng. Dynamics of immiscible-fluid displacement in a capillary tube. *Phys. Rev. Lett.*, 64:882–885, 1990.